JOURNAL OF GEOPHYSICAL RESEARCH, VOL. 108, NO. D12, 4345, doi:10.1029/2002JD002918, 2003

Saharan dust over a central European EARLINET-AERONET site: Combined observations with Raman lidar and Sun photometer

Detlef Müller, Ina Mattis, Ulla Wandinger, Albert Ansmann, and Dietrich Althausen
Institute for Tropospheric Research, Leipzig, Germany

Oleg Dubovik
NASA Goddard Space Flight Center, Greenbelt, Maryland, USA

Sabine Eckhardt and Andreas Stohl
Lehrstuhl für Bioklimatologie und Immissionsforschung, Technical University of Munich, Freising, Germany

Received 6 September 2002; revised 4 November 2002; accepted 16 December 2002; published 17 June 2003.

[1] Combined observations with an advanced aerosol water-vapor temperature Raman lidar and a Sun photometer are used for a detailed characterization of geometrical and optical properties of a continental-scale Saharan dust event observed over Leipzig (51.3°N, 12.4°E), Germany, from 13 to 15 October 2001. The Raman lidar is part of the European Aerosol Research Lidar Network (EARLINET). Automatic observations of aerosol optical depth and sky brightness are made with the Sun photometer in the framework of the worldwide operating Aerosol Robotic Network (AERONET). The dust plume reached a top height of 6000 m. Sun photometer and lidar observations showed a constant increase of columnar optical depth at 532 nm from 0.25 on 13 October 2001 to a maximum of ~0.63 on 14 October 2001. According to observations with lidar, up to 90% of the optical depth at the wavelength of 532 nm was contributed by the dust layer above 1000-m height. Ångström exponents from Sun photometer observations between 380 and 1020 nm were ~0.45 at the beginning of the dust period, and dropped to minimum values of 0.14 during the peak of the dust outbreak. Vertically resolved Ångström exponents derived from lidar profiles of the extinction coefficients at 355 and 532 nm showed a strong variability with values as low as −0.2 in the center of the dust plume. Below 1000-m height column-averaged Ångström exponents strongly varied between 1.0 in the beginning of the dust period and 0.39 on 14 October 2001 when the dust penetrated into the boundary layer. Comparison of column-averaged optical depth and Ångström exponents derived from lidar and Sun photometer observations showed excellent agreement. Particle depolarization ratios of up to 25% were derived from lidar observations at 532 nm. Scattering phase functions retrieved from Sun photometer observations indicated particles of nonspherical shape. This shape caused unusually large particle extinction-to-backscatter (lidar) ratios at 532 nm in the range from 50 to 80 sr. There were substantial deviations of the lidar ratio at 532 nm derived from both measurement methods. They are explained by the effect of particle shape. *INDEX TERMS:* 0305 Atmospheric Composition and Structure: Aerosols and particles (0345, 4801); 0360 Atmospheric Composition and Structure: Transmission and scattering of radiation; 1630 Global Change: Impact phenomena; 1640 Global Change: Remote sensing; *KEYWORDS:* microphysical properties, optical properties, Raman lidar, Saharan dust, Sun photometer

Citation: Müller, D., I. Mattis, U. Wandinger, A. Ansmann, D. Althausen, O. Dubovik, S. Eckhardt, and A. Stohl, Saharan dust over a central European EARLINET-AERONET site: Combined observations with Raman lidar and Sun photometer, *J. Geophys. Res.*, *108*(D12), 4345, doi:10.1029/2002JD002918, 2003.

1. Introduction

[2] *Mattis et al.* [2002b] reported on unusually large lidar ratios of Saharan dust particles observed over Leipzig (51.3°N, 12.4°E), Germany. A first analysis of this dust outbreak, which lasted from 13 to 15 October 2001, showed that these large lidar ratios most likely were caused by the nonspherical shape of the dust particles. In this contribution we extend the analysis of the geometrical and optical properties of this dust plume. For this purpose we present for the first time a detailed characterization of a Saharan

0148-0227/03/2002JD002918$09.00

dust plume using combined observations with an advanced two-wavelength aerosol water-vapor temperature Raman lidar and a CIMEL Sun photometer (Cimel Electronique, Paris, France). Both instruments are operated at the Institute for Tropospheric Research (IfT) in Leipzig. The Raman lidar is involved in regular measurements within the European Aerosol Research Lidar Network (EARLINET) [*Bösenberg et al.*, 2001], which consists of 22 lidar stations in 13 European countries. Since February 2000 regular lidar observations are done three times a week to derive a vertically resolved aerosol climatology over Europe. The CIMEL Sun photometer is part of the worldwide operating Aerosol Robotic Network (AERONET), which started regular observations in 1993 [*Holben et al.*, 1998]. AERONET provides column-averaged aerosol optical and microphysical properties for different regions of the world [*Dubovik et al.*, 2002a].

[3] One of the key issues of EARLINET is the observation of transport of Saharan dust across Europe. According to the latest report by the *Intergovernmental Panel on Climate Research* (*IPCC*) [2001], dust causes large uncertainties with respect to the assessment of climate forcing by atmospheric aerosols. These uncertainties exist with respect to production, particle properties, transport paths, and evolution during the particles' life time. Model studies suggest that the direct radiative forcing of dust on a regional as well as on the global scale may be comparable to or even exceed the forcing by anthropogenic aerosols [*Tegen and Fung*, 1995; *Li et al.*, 1996; *Sokolik and Toon*, 1996; *Tegen et al.*, 1996]. Observations indicate a large seasonal variability of the dust cycle that is strongly correlated with the global atmospheric circulation [*Moulin et al.*, 1997]. The first two years of regular observations by the EARLINET stations showed frequent transport of Saharan dust from southern Europe to central and northern Europe. It has been shown that dust plumes may be found in heights well above the surface [*Hamonou et al.*, 1999; *Gobbi et al.*, 2000; *Di Sarra et al.*, 2001; *Mattis et al.*, 2002b; *Welton et al.*, 2000]. Observations of mineral dust in different parts of the Mediterranean region revealed significantly different optical properties, as the result of highly variable physical and chemical properties [e.g., *Sokolik et al.*, 1998; *von Hoyningen-Huene et al.*, 1999; *Tanré et al.*, 2001].

[4] Remote-sensing techniques such as lidar and Sun photometer provide particle information mostly inaccessible to in situ instrumentation. Although in situ observations at the surface give a detailed and long-term monitoring of chemical and physical characteristics these observations are not very representative of the particle conditions in the free troposphere. In situ observations with aircraft can only provide short-term monitoring during field campaigns [e.g., *Öström and Noone*, 2000; *Schmeling et al.*, 2000; *Haywood et al.*, 2001]. The well-known particle losses caused by the instrument inlets, in particular with respect to large mineral dust particles, may cause severe biases of derived optical properties of particles.

[5] The Raman lidar at IfT currently is the only EARLINET station that simultaneously provides important optical aerosol parameters, that is, profiles of backscatter coefficients, extinction coefficients, and of lidar ratios at multiple wavelengths, and the particle depolarization ratio, in combination with important meteorological parameters, that is, profiles of temperature and of relative humidity [*Mattis et al.*, 2002a]. Accurate profiles of particle extinction coefficients, and thus of optical depth, are determined at the wavelengths of 355 and 532 nm [*Mattis*, 2002; *Mattis et al.*, 2002a]. Wavelengths in the ultraviolet part of the spectrum are particularly important as mineral dust is highly absorbing in this wavelength range compared to wavelengths in the visible part of the spectrum [*Patterson et al.*, 1977; *d'Almeida et al.*, 1991].

[6] Profiles of Ångström exponents are derived from the extinction coefficients. Ångström exponents are a good indicator of the size of the observed particles [*Ångström*, 1964; *Reid et al.*, 1999; *O'Neill et al.*, 2001a; *Ansmann et al.*, 2002; *Müller et al.*, 2002].

[7] Raman measurements are most sensitive under nighttime conditions, because of the reduced background signal from sunlight. In this study we also present extinction profiles derived from Raman signals detected under daytime conditions. Consequently, optical depths can be directly compared to respective measurements with Sun photometer. The spectral measurements allow us to determine Ångström exponents for different wavelength ranges. Measurements of sky brightness under different azimuth angles provide important information on particle shape [*Wendisch and von Hoyningen-Huene*, 1992]. In addition, microphysical particle properties may be determined [*Dubovik and King*, 2000].

[8] Two strong events, in terms of observed particle optical depths and spatial and temporal extension, of transport of Saharan dust across Europe in August 2001 and October 2001 were observed at the EARLINET-AERONET site [*Mattis et al.*, 2002b]. Both events were observed at most of the other EARLINET stations. Observations made by the Total Ozone Mapping Spectrometer (TOMS) indicated a comparably high aerosol load over Germany on 13 and 14 October 2001. The high optical depths during the dust outbreak in October 2001 were most favorable for highly accurate retrievals of particle properties. The combination of both instruments allowed to monitor of aerosol properties under nighttime as well as daytime conditions.

[9] Cloud-free conditions prevailed during the observations in the morning of 14 October 2001, whereas cirrus clouds moved into the observational area in the afternoon of 14 October 2001 and remained there for the rest of the dust event. The morning of 14 October 2001 therefore was most favorable for a rigorous quality assessment of the derived aerosol properties. Deficiencies of both instruments, for example, column-averaged information from measurements by Sun photometer and restriction to minimum measurement heights for lidar, could be compensated for with the combined observations. Section 2 describes the instruments and the data sets. Section 3 presents the measurements. In section 4 we discuss the findings. A summary is given in section 5.

2. Methodology

2.1. EARLINET Raman Lidar

[10] An overview of the Raman lidar is given by *Mattis* [2002] and *Mattis et al.* [2002a]. The stationary instrument emits laser pulses at 355, 532, and 1064 nm by means of one Nd:YAG laser. The pulse repetition rate is 30 Hz. The overall output power is $\sim$1.6 J per pulse. The laser beam is

expanded tenfold before it is emitted vertically into the atmosphere. The backscattered light is collected with a 1-m Cassegrain telescope. Elastically backscattered signals are collected at the three emitted wavelengths. The signal cross-polarized with respect to the state of polarization of the emitted light is detected at 532 nm. Signals inelastically backscattered from nitrogen molecules are detected at 387 and 607 nm. Signals at 407 nm follow from Raman scattering by water-vapor molecules. The separation of wavelengths is done with dichroic beam splitters and interference filters. Signals at 529.0, 530.3, 533.8, and 535.2 nm are separated from the pure rotational Raman spectrum of nitrogen molecules with a double-grating monochromator [*Arshinov et al.*, 1983]. A Fabry-Perot etalon is used to suppress the daylight background in between the rotational Raman lines [*Arshinov and Bobrovnikov*, 1999; *Arshinov et al.*, 2001; *Bobrovnikov et al.*, 2002].

[11] Particle extinction profiles are derived with high accuracy from the nitrogen Raman signals [*Ansmann et al.*, 1990] under nighttime conditions. A rigorous error analysis can be found elsewhere [*Ansmann et al.*, 1992a; *Ferrare et al.*, 1998; *Masonis et al.*, 2002]. Below ~3-km height the incomplete overlap between the emitted laser beam and the receiver's field of view affects the accuracy of the extinction profiles. The application of a so-called overlap function, which is determined experimentally [*Wandinger and Ansmann*, 2002], allows one to retrieve profiles to a minimum height of ~1 km. In this height range errors can increase to 50%. Further systematic errors, for example, the assumption of the wavelength dependence of the extinction between the emitted wavelength and the Raman-shifted wavelength and uncertainties in the assumed density profile of the atmosphere [*Ansmann et al.*, 1992a, 1992b], in summary are <5% and thus of minor importance. Statistical errors are on the order of 10% for the Saharan dust plume presented in this paper [*Mattis et al.*, 2002b].

[12] During the period of high optical depth Raman signals at 387 nm detected under daylight conditions with interference filters of 3-nm bandwidth were used for the determination of the extinction coefficient at 355 nm. Extinction profiles were determined throughout the dust plume, which reached to a height of ~4000 m at that time (cf. Figure 1). Errors for the daytime profiles were ~10% in the dust layer below 3800-m height. Above that height the uncertainty strongly increased.

[13] Extinction profiles at 532 nm under daylight conditions were determined on the basis of the pure rotational Raman lines. These signals until now were only used for the retrieval of temperature profiles [*Arshinov et al.*, 2001; *Bobrovnikov et al.*, 2002; *Mattis et al.*, 2002a]. In that case the temperature dependence of the signals at the different wavelengths was used. For the retrieval of the daytime profiles of the particle extinction coefficient all four Raman signals were added up to one signal. A sensitivity analysis showed a negligible temperature dependence of the signal obtained in that way. Because of the efficient suppression of the daylight background with the Fabry-Perot interferometer the signals can be detected throughout the entire troposphere. Uncertainties of the extinction profiles are comparable to those from the nighttime observations, which are based on the vibrational Raman signals.

[14] The particle backscatter coefficients at 355 and 532 nm are calculated with high accuracy with the Raman method [*Cooney et al.*, 1969; *Ansmann et al.*, 1992b]. The elastic signals at 355 and at 532 nm and the inelastic signals at 387 and at 607 nm from Raman scattering by nitrogen molecules are used. As in the case of the extinction profile at 532 nm the backscatter profile at 532 nm under daylight conditions was also retrieved with the help of the rotational Raman signals around 532 nm.

[15] The Raman method for the backscatter coefficients uses signal ratios only. Therefore the overlap effect is cancelled out, and the respective profiles can be retrieved to a minimum height of 60 m above the surface. The major error source is the assumption of the particle backscatter coefficient in a specific reference height. This error, the uncertainties of the wavelength dependence of the extinction coefficients between emitted and Raman-shifted wavelength and of the atmospheric density profile add up to <5% for the measurements presented here. A detailed description of the error analysis for the Raman method is given elsewhere [*Ansmann et al.*, 1992a; *Ferrare et al.*, 1998; *Franke et al.*, 2001; *Masonis et al.*, 2002].

[16] Particle backscatter coefficients at 532 nm describing daytime conditions were also retrieved without the use of Raman signals. For this purpose the so-called Klett method [*Klett*, 1981; *Fernald*, 1984; *Evans*, 1988] is used. This method is less accurate because it requires the a priori assumption of the particle extinction-to-backscatter (lidar) ratio. Errors may exceed 20% [*Sasano et al.*, 1985]. As in the case of the extinction profiles the minimum height for the retrieval of profiles is determined by the overlap effect.

[17] The lidar ratios at 355 and 532 nm are determined directly from the extinction and backscatter coefficients derived with the Raman method at the respective wavelengths. Errors are largely determined by the uncertainties of the extinction profiles and add up to $\leq$15% [*Mattis et al.*, 2002b].

[18] The Ångström exponent å [*Ångström*, 1964] is derived from the extinction coefficients. This parameter is most commonly used for the qualitative description of mean particle size. In the present case,

$$\mathring{a}_{\lambda_1,\lambda_2}(z) = -\frac{\ln[\alpha_{\lambda_1}(z)/\alpha_{\lambda_2}(z)]}{\ln(\lambda_1/\lambda_2)} \quad (1)$$

describes the spectral slope of the spectrum of the measured extinction coefficients α_λ at the wavelengths λ_1 = 355 nm and λ_2 = 532 nm. The uncertainties are determined by the errors of the individual profiles.

[19] The depolarization properties of the particles are determined at 532 nm. The particle depolarization ratio is defined as the ratio of the cross-polarized to the parallel component of the particle backscatter coefficient at 532 nm [*Cairo et al.*, 1999; *Murayama et al.*, 1999]. A detailed error analysis can be found in, for example, *Cairo et al.* [1999].

[20] The relative humidity was determined from measurements of the water-vapor mixing ratio with lidar and profiles of temperature determined from radiosonde ascents. For the water-vapor mixing ratio the ratio of the signals from Raman scattering from water-vapor and nitrogen molecules is used [*Melfi et al.*, 1969; *Cooney*, 1970; *Melfi*, 1972]. Because of the use of signal ratios the overlap effect is

cancelled out. A detailed error analysis is given elsewhere [*Melfi et al.*, 1969; *Ansmann et al.*, 1992a].

2.2. AERONET Sun Photometer

[21] The instrument is a robotically operated Sun and sky spectral radiometer. The full-angle field of view is $\sim 1.2^\circ$. Two detectors are used for the measurement of direct Sun, aureole, and sky radiance. Spectral observations of Sun and aureole radiance are made at 340, 380, 440, 500, 670, 870, 940, and 1020 nm. Measurements of sky radiance are made at 440, 670, 870, and 1020 nm. Details of the calibration procedure are given elsewhere [*Holben et al.*, 1998, 2001].

[22] The columnar optical depth is determined at the measurement wavelengths except for the channel at 940 nm. This channel is used for the retrieval of columnar precipitable water. Ångström exponents are determined from optical depth according to equation (1). If particle size distributions consist of fine particles (particle radius ≤ 0.5 μm) and of particles in the coarse mode (particle radius ≥ 0.5 μm) the use of Ångström exponents in different wavelength ranges is of advantage. Ångström exponents for short wavelengths are sensitive to small particles whereas the Ångström exponents at long wavelength give a qualitative description of large particles [e.g., *Reid et al.*, 1999; *O'Neill et al.*, 2001a, 2001b; *Ansmann et al.*, 2002].

[23] Particle phase functions at 440, 670, 870, and 1020 nm are derived from measurements of sky brightness. For this purpose the measured sky brightness is modeled with a Mie code and radiative-transfer calculations [*Dubovik and King*, 2000; *Dubovik et al.*, 2000]. Input for the model are the Sun radiances and the angular distribution of sky radiance in the solar almucantar. The method attempts to fit the measured spectral and multiangle Sun and sky radiances at 440, 670, 870, and 1020 nm by selecting appropriate phase functions, single-scattering albedos, and optical depths. The range of these parameters is constrained by a simultaneous search of the particle size distribution in the particle radius range from 0.05 to 15 μm and the particle complex refractive index, which is assumed to be wavelength dependent. The used radiative-transfer model employs a discrete-ordinates code that accounts for multiple scattering effects [*Nakajima and Tanaka*, 1988]. The model further includes effects by Rayleigh scattering, gas absorption, and surface reflectance. Spectral and size smoothness are used as constraints.

[24] The model assumes homogeneous composition of the detected particles. The column-integrating measurement method simultaneously detects mixtures of different particle types, for example, particles in the planetary boundary layer and in the free troposphere. Widely different particle properties in the fine and in the coarse mode may be present. Sensitivity studies showed that for such external mixtures of particles the retrieved complex refractive indices have effective values in between those assumed for the inhomogeneous spheres [*Dubovik et al.*, 2000].

[25] The most crucial assumption made for the algorithm in the present case is the spherical shape of the scatterers. Lidar observations showed that the detected dust particles were highly depolarizing. Numerical simulations [*Dubovik et al.*, 2000] and results from AERONET observations of desert dust [*Dubovik et al.*, 2002a] showed that the assumption of spherical scatterers produces two distinct artifacts in the retrieval of nonspherical particles of desert dust. There is an unrealistically high concentration of small particles with radius ≤ 0.1 μm. Further the real part of the complex refractive index shows an unrealistic spectral dependence. These artifacts can be eliminated if dust particles are treated as randomly oriented spheroids, similarly to the model developed by *Mishchenko et al.* [1997]. A detailed description can be found in *Dubovik et al.* [2002b].

[26] Briefly, this extended version of the retrieval scheme describes the particles as spheroids of oblate and prolate shape with given aspect ratio ϵ_P from 1.6 to 2.2. The aspect ratio is defined as the ratio of the length of the long axis to the length of the short axis of the particles. Further assumption is that the spheroids of all sizes have the same distribution of aspect ratios. Accordingly the weighting function $w(\epsilon_P)$ is set to

$$\sum_{\epsilon_P} w(\epsilon_P) = 1. \tag{2}$$

[27] A maximum particle radius of 15 μm is considered. This number transforms to size parameters from 0.3 to 215 for the measurement wavelength range from 440 to 1020 nm, which is much larger than the maximum values of 40–60 considered by *Mishchenko et al.* [1997]. Above size parameters of 40–60, for which the method by *Mishchenko et al.* [1997] becomes numerically unstable, an approximate method was used [*Yang and Liou*, 1996].

[28] The present measurement case offered the opportunity to test the validity of the model assumption of spherical or nonspherical shape of the scatterers. For this purpose a comparison was made for the particle lidar ratio on the basis of the lidar measurements, for which no model assumptions are made, and on the basis of the Sun photometer observations.

[29] As outlined by several authors [*Mishchenko et al.*, 1997; *Liu et al.*, 2002; *Mattis et al.*, 2002b] the nonspherical geometry of particles leads to a strong increase of the particle lidar ratio compared with the value obtained from respective spherical scatterers. This increase is caused by a significant reduction of the particle backscatter coefficient. In contrast, the particle extinction coefficient is sensitive to the cross-section of the particles and thus affected by particle shape much less [*Mishchenko et al.*, 1997]. The calculation of the column-averaged lidar ratio $S(\lambda)$ at a given wavelength from Sun photometer needs the particle phase function as input parameter, and thus also is strongly influenced by particle shape. In dependence of the model used for the inversion of the Sun photometer data there should be a significant change in the particle phase function. The lidar ratio $S(\lambda)$ is calculated according to the following equations:

$$S(\lambda) = \frac{\alpha(\lambda)}{\beta(\lambda)} = \frac{4\pi}{\omega(\lambda) P(\lambda, 180^\circ)}, \tag{3}$$

$$\frac{1}{2}\int_0^\pi \sin(\Theta) P(\lambda, \Theta) d\Theta = 1, \tag{4}$$

$$\omega(\lambda) = \frac{\int_{r_{\min}}^{r_{\max}} C_{\text{sca}}(\lambda, r) n(r) dr}{\int_{r_{\min}}^{r_{\max}} C_{\text{ext}}(\lambda, r) n(r) dr}. \tag{5}$$

[30] The terms $\alpha(\lambda)$ and $\beta(\lambda)$ describe the particle extinction coefficient and the particle backscatter coefficient determined with lidar, respectively. The single-scattering albedo $\omega(\lambda)$ and the particle phase function $P(\lambda, 180°)$ at 180° follow from the inversion of the Sun photometer data. Θ is the scattering angle. The term $C_{sca}(\lambda, r)$ describes the particle scattering cross section, and $C_{ext}(\lambda, r)$ is the particle extinction cross section, for given particle radius r and wavelength λ. The column-averaged particle number size distribution is denoted by $n(r)$ and results from the inversion of the Sun photometer data. r_{min} and r_{max} denote minimum and maximum particle radius, respectively, of the particle size distribution. Similar to the particle extinction coefficient, the particle scattering coefficient and single-scattering albedo are sensitive to the cross section of the particles and thus only slightly affected by particle shape [*Mishchenko et al.*, 1997].

[31] Extensive sensitivity studies that describe the accuracy of the retrieved microphysical properties can be found in *Dubovik et al.* [2000, 2002b]. The error analysis showed that the complex refractive index can be quite accurately determined for high aerosol optical depths $\geq$0.5 at 440 nm and for measurements under solar zenith angles >50°. Errors for the imaginary part are 30%–50%. The error for the real part is ~0.04. For optical depths $\leq$0.2 at 440 nm the accuracy drops to 80%–100% for the imaginary part of the complex refractive index, and to 0.05 for the respective real part.

[32] The particle volume size distribution does not suffer from limitations of optical depth, if it is $\geq$0.05 at 440 nm [*Dubovik et al.*, 2000]. In the size range from 0.1 to 7 μm the uncertainty is <10% in the respective maxima of the size distribution. For multimodal size distributions uncertainties are as large as 35% in the minima of the respective size distribution. At the edges of the size distributions errors rise to 80%–100% if particle size is <0.1 μm and >7 μm, respectively.

[33] Minimum values of the residual, which is determined by the best fit of the measured radiances to the used theoretical model, are sensitive to experimental errors and the failure of the radiative model. In the absence of strong systematic biases the errors add up to 5%–7%. Errors of the phase functions at 180° may easily reach 50% if the wrong model for particle shape is taken.

[34] It has to be observed that the above given levels of accuracy are valid for cloud-free conditions. Next to the ability to accurately test cloud-free conditions with lidar, the AERONET inversion algorithm also uses a cloud-screening procedure. The sky radiance measured in the solar almucantar is checked for symmetry. For a spatially homogeneous atmosphere the sky radiances in the left and right part of the almucantar should be very similar. If this requirement is not fulfilled the respective measurement is omitted in data analysis.

3. Measurement

3.1. Lidar Observations

[35] Figure 1 shows the particle backscatter coefficient at 532 nm for several measurement periods between 1706 UTC on 12 October and 1936 UTC on 15 October 2001. The individual profiles were determined with the Klett method.

[36] Figure 2 shows the time series of the profiles of the particle backscatter coefficients and particle extinction coefficients, of the Ångström exponent, and of the particle lidar ratio at 532 nm. The measurements were done after sunset on 13 October 2001, around noontime on 14 October, and again after sunset on 14 October 2001. A brief discussion of the profiles of the backscatter coefficients and the lidar ratios taken at nighttime on 13 October 2001 and on 14 October 2001 can be found in *Mattis et al.* [2002b].

[37] Figure 3 shows the time series of 10-day backward trajectories arriving at 1800 UTC on 13 October 2001 and at 1200 UTC and at 1800 UTC on 14 October 2001. The backward trajectories were calculated with the 3-dimensional trajectory model FLEXTRA [*Stohl et al.*, 1995]. Global model-level wind fields of the spectral model T511 L60 of the European Centre for Medium-Range Weather Forecasts (ECMWF) [*ECMWF*, 1995] were used as input for FLEXTRA. The ECMWF data used had a resolution of 1° latitude × 1° longitude and a temporal resolution of 3 hours (analyses at 0, 6, 12, and 18 UTC; 3-hour forecasts at 3, 9, 15, and 21 UTC).

[38] According to this time series the north African desert regions between 10°N and 35°N and between 15°W and 25°E most likely were the source regions of the observed aerosol layers. Measurements by other lidar stations of EARLINET indicated an extension of this Saharan dust plume on the continental scale.

[39] Faint traces of dust were observed in heights between 4000 and 6000 m in the evening of 12 October 2001. The measurement between 1142 and 1253 UTC on 13 October 2001 showed the Saharan dust layer between ~1000- and 6000-m height. Cirrus was detected in heights between 10 and 12 km (see Figure 1).

[40] In comparison to the daytime observations considerably larger particle backscatter coefficients were observed in the nighttime measurement from 1729–2007 UTC on 13 October 2001. The layer of strong backscatter coefficients that had appeared after 1215 UTC on that day had increased in vertical extension. The center of the dust plume had descended from ~3500-m height to 3000-m height between the two observational periods. The descent was caused by a high-pressure system over south and southeast Europe. Backward trajectories for arrival heights between 2000 and 3000 m show that the airmass was close to the surface in the source regions (see Figure 3a). An accumulation of mineral particles in this airmass therefore is most likely. Particle backscatter coefficients in the central portion of the dust plume were as high as 5 $Mm^{-1}sr^{-1}$.

[41] The transition to the boundary layer, indicated by comparably low backscatter coefficients, is around 800-m height. Below that height the particle backscatter coefficient shows maximum values between 1 and 2 $Mm^{-1}sr^{-1}$. According to the backward trajectories the airmass that arrived in 500-m height above the lidar site had originated over the North Atlantic and then crossed southwest Europe (see Figure 3a) mostly above 2-km height. During the last 4 days before observation the airmass mixed with airmasses that had originated in the Sahara region. Therefore an accumulation with mineral particles cannot be ruled out. Sedimentation of, in particular, large particles from one airmass into another airmass may have occurred as well. An accumulation with particles from anthropogenic pollution in

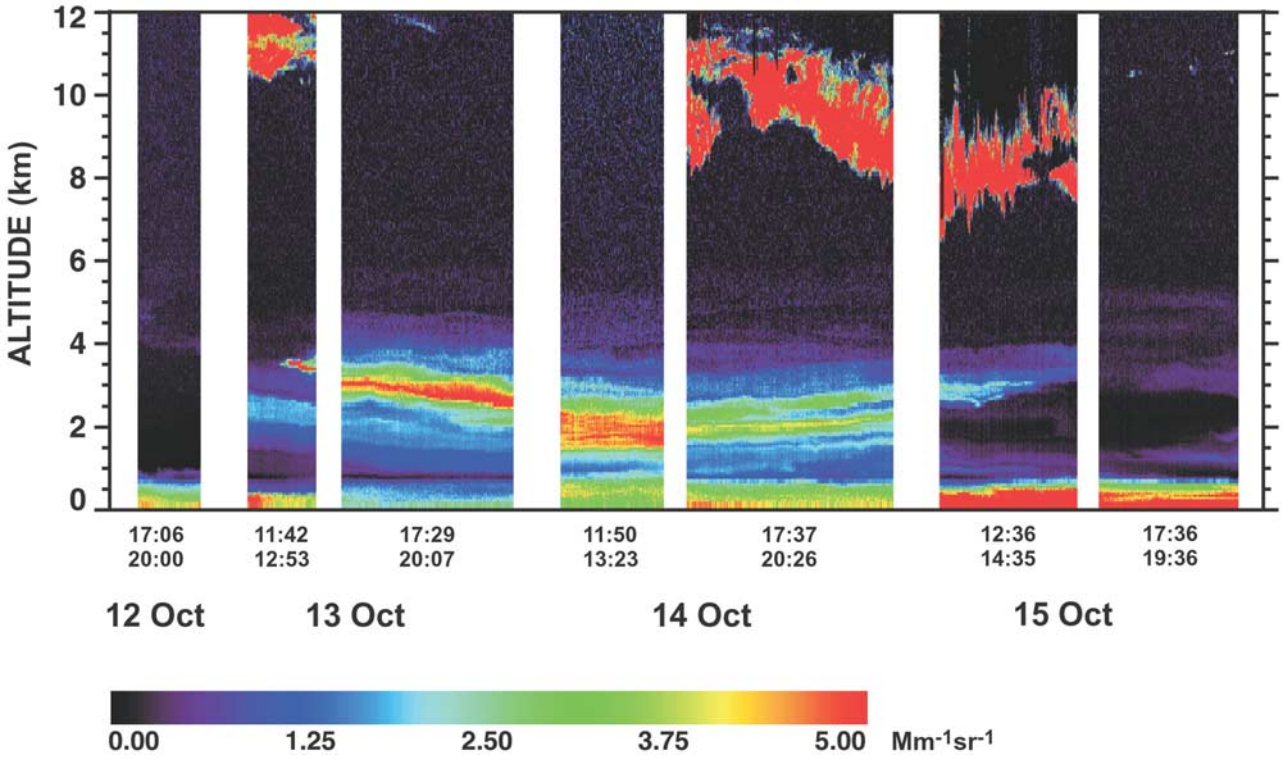

Figure 1. Time series of the particle backscatter coefficient at 532 nm between 1706 UTC on 12 October 2001 and 1936 UTC on 15 October 2001. Temporal resolution of the individual profiles is 30 s, the spatial resolution is 60 m.

the boundary layer may have occurred during the last 48 hours prior to the lidar observation when the airmass descended to heights below 2 km. Only faint traces of cirrus were seen in 11.5-km height around 1830 UTC.

[42] The measurement from 1150 to 1323 UTC on 14 October 2001 shows the penetration of the dust plume into the planetary boundary layer. The clear separation between aerosols in the free troposphere and aerosols in the boundary layer had disappeared. The center of the dust plume had descended to heights of ~2 km. Backward trajectories in this height range show the advection of airmasses from North Africa (see Plate 3b). The airmass was close to the surface over the source region for several days.

[43] A factor of 2 larger backscatter coefficients compared to the conditions on the previous evening were found in the planetary boundary layer below ~500-m height. The backward trajectory with arrival height of 500 m shows that the respective airmass had originated from ~5.5-km height over the Sahara. During the descent the airmass most likely mixed with other airmasses of high particle content in the last 6 days prior to observation, as can be seen from the respective backward trajectories and the backscatter coefficients (see Figures 1 and 3b). Ground-based in situ observations with particle counters located at IfT showed increasing concentrations of particles in the coarse mode during the dust event (B. Wehner, personal communication, 2002). Size-resolved measurements of particle concentration at about 700-m height on a mountain ~150 km southwest of IfT also showed a significant increase of large particles (S. Mertes, personal communication, 2002).

[44] In comparison to the conditions around noon particle backscatter coefficients in the free troposphere on average were lower during the nighttime measurement from 1737 to 2026 UTC. The maximum values still were found around 2-km height. Backscatter values within the planetary boundary layer on average had slightly increased compared to the observations at noontime. Backward trajectories showed that the airmass with arrival height at 2 km had been close to the surface over the source region in the western part of the Sahara (see Figure 3c). Backscatter coefficients further decreased on 15 October 2001. The afternoon measurement on 16 October 2001 finally showed almost particle-free conditions in the free troposphere (not shown in Figure 1).

[45] Figure 2b shows that extinction coefficients at 532 nm were highly variable, with values between 50 and 250 Mm^{-1} in the lofted particle layer. Optical depth of the dust plume above 1000-m height slightly increased from 0.42 during the observations after sunset on 13 October 2001 to 0.48 at noon on 14 October 2001 and then decreased to 0.33 during the nighttime observations on 14 October 2001.

[46] Mean extinction below ~1000-m height was 40–60 Mm^{-1} on 13 October 2001. Accordingly optical depth was 0.04–0.06 for the lowermost 1000 m of the troposphere. The coefficients were calculated on the basis of the profiles of the particle backscatter coefficient at 532 nm, integrated from the surface to 1000-m height, and under the assumption of a lidar ratio of 40 and 60 sr at 532 nm, respectively. As can be seen from Figure 2d, the lidar ratio varied within this range at ~1000-m height. 40–60 sr is also the typical range of values for the lidar ratio of boundary-layer aerosols

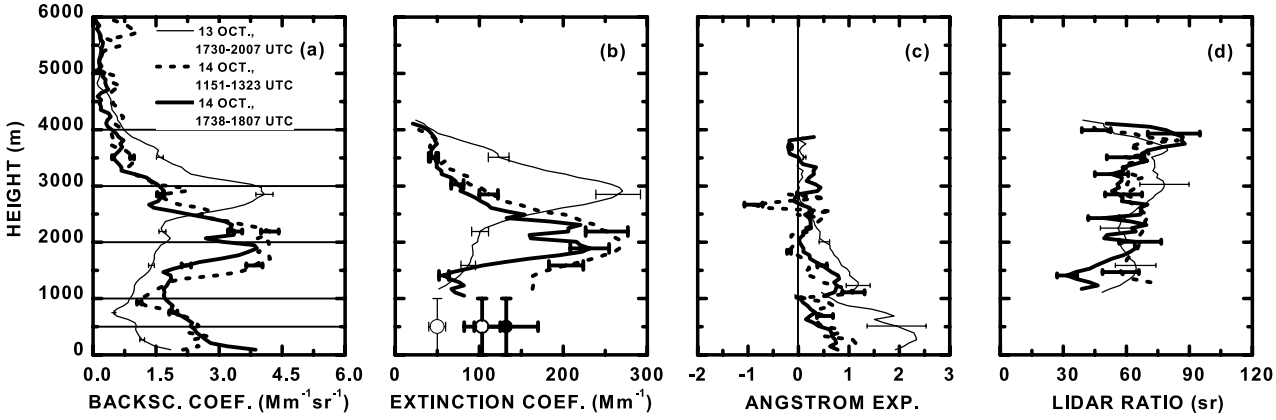

Figure 2. Time series of profiles of the particle backscatter coefficient at 532 nm (Figure 2a), the particle extinction coefficient at 532 nm (Figure 2b), and the Ångström exponent (Figure 2c) for the wavelength range from 355 to 532 nm based on the extinction profiles. Below 1000-m height Ångström exponents were calculated from respective profiles of the backscatter coefficients and the assumption of a wavelength-independent lidar ratio of 60 sr. The time series of the lidar ratio at 532 nm is shown in Figure 2d. Also shown are column-averaged extinction coefficients from 0 to 1000-m height on 13 October 2001 (open thin circle), at noontime on 14 October 2001 (open thick circle), and at nighttime on 14 October 2001 (closed circle). The vertical resolution of the profiles of the backscatter coefficient is 60 m. The nighttime profiles of the extinction coefficients at 355 (not shown) and 532 nm, of the Ångström exponents, and of the lidar ratios were smoothed with an averaging length of 660 m. The respective daytime profiles were smoothed with an averaging length of 660 m below 3800-m height and 1260 m above 3800-m height. For the calculation of the lidar ratio the backscatter profiles were smoothed with the same averaging lengths as the extinction profiles. Horizontal lines in Figure 2a denote the arrival heights of the backward trajectories shown in Figure 3. For clarity the value of 0 for the Ångström exponents is denoted by a vertical line.

observed over Leipzig during the EARLINET observations. Mean extinction coefficients within the boundary layer increased by a factor of 2 between 13 and 14 October 2001. Accordingly optical depth within the lowermost 1000 m increased to 0.08–0.12 at noontime on 14 October 2001. This increase most likely was caused by an increased concentration of mineral particles in the boundary layer. Comparably large extinction values were present during the evening observation.

[47] Figure 2c shows the time series of the profile of the Ångström exponent on the basis of the extinction profiles at 355 and 532 nm. Below 1000-m height the respective extinction profiles were obtained from the backscatter profiles and the assumption of a wavelength- and height-independent lidar ratio of 60 sr.

[48] For the retrieval of the Ångström exponents under daylight conditions the respective extinction profiles at 355 and 532 nm had to be determined. In the case of the profile at 532 nm the error of the extinction was low because of the use of the rotational Raman lines. The maximum height for trustworthy values of the extinction profile at 355 nm was 4000 m. This top height includes the major portion of the dust plume for that specific timeframe. The uncertainty on average was 10%. A quality test of the profile was done through a comparison of optical depth derived from this profile to optical depth determined with Sun photometer. The Sun photometer value was 0.62, which is ~10% less than the value of 0.69 derived from lidar.

[49] The Ångström exponents for the dust plume above 1000-m height varied between −0.2 and 1.2, which points to rather large particles in the dust plume. There is a steady increase of the Ångström exponent with decreasing height on 13 October 2001. In the planetary boundary layer the Ångström exponent reached a maximum value of 2.0, which indicates rather small particles. On 14 October 2001, the profiles of the Ångström exponent did not show this pronounced height dependence. The Ångström exponents varied between 0 and 1 in the dust plume down to the surface, and thus on average were lower than on the previous day. In the nighttime observation of 14 October 2001 the increased concentration of dust particles in the boundary layer had become so strong that the clear separation between aerosols in the free troposphere and in the planetary boundary layer had disappeared.

[50] Figure 2d shows that the lidar ratio at 532 nm on average varied between 50 and 80 sr throughout the observational period. A further discussion of the particle lidar ratio at 532 and at 355 nm for the nighttime measurements on 13 October 2001 and 14 October 2001 is given by *Mattis et al.* [2002b].

[51] Figure 4 shows the time series of the particle depolarization ratio at 532 nm for the time frames given in Figure 2. On 13 October 2001 the transition from the dust plume to the aerosols in the boundary layer below 1000-m height can be easily recognized. There is a sharp drop of the depolarization ratio at 532 nm from 20% to 25% to minimum values of 5%. Interestingly, the measurement at noon on 14 October 2001 showed lower depolarization ratios of 10%–20% in the dust plume in the free troposphere compared to the conditions on 13 October 2001. The sharp drop to values characteristic for particles from anthropogenic pollution occurs around 500-m height. The

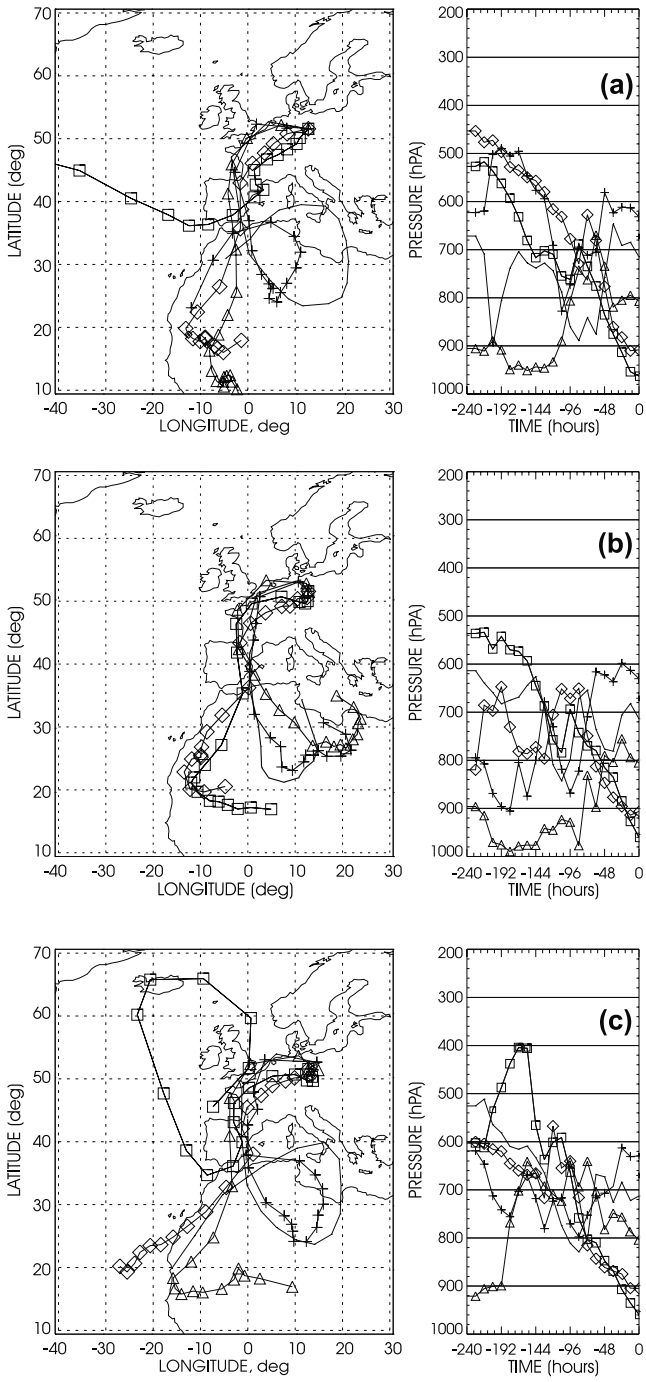

Figure 3. Ten-day backward trajectories for arrival heights of 500, 1000, 2000, 3000, and 4000-m height over the lidar site (right panel, time 0, from bottom to top). Arrival times are 1800 UTC on 13 October 2001 (Figure 3a) and 1200 and 1800 UTC on 14 October 2001 (Figures 3b and 3c, respectively). The left panel presents the horizontal projection of the trajectories with their positions marked every 12 hours.

nighttime observation again showed large depolarization ratios of 20%–25%. Large depolarization ratios above 10% were present almost down to the surface, thus indicating that the boundary layer contained a high concentration of particles of nonspherical geometry.

[52] Figure 5 shows the profiles of potential temperature determined from radiosonde ascents (Vaisala RS-80). Relative humidity was determined from the radiosonde temperature profiles in combination with the lidar profiles of the water-vapor mixing ratio. Shown for comparison is relative humidity determined with radiosonde.

[53] The profile of potential temperature between 1730 and 2007 UTC shows stable atmospheric conditions throughout the troposphere except below ~200-m height on 13 October 2001. A rather stable stratification was observed below 500-m height on 14 October 2001. In terms of potential temperature the airmasses in the free troposphere were 10–25 K warmer than the air in the boundary layer. A temperature inversion at ~800-m height indicates the top of the planetary boundary layer (see Figure 1).

[54] The relative-humidity profile indicates the top of the dust layer at ~6000-m height. Values drop from ~60% to 30% between 5500 and 6000-m height. Relative humidity was 45%–60% in most parts of the dust plume. The transition to the boundary layer at 800-m height is indicated by a drop of relative humidity to ~30%. The relative error of relative humidity was below 5% below 6000-m height. The water-vapor mixing ratio showed highly stable conditions during the observational period.

3.2. Sun Photometer Observations

[55] Figure 6 presents the time series of optical depth at 380 nm and at 1020 nm on the basis of the Sun photometer observations and the time series of the column-averaged Ångström exponent for the respective wavelength range. The timeframe is from 0716 UTC on 13 October 2001 until 1437 UTC on 14 October 2001 (286.30–287.61 Julian day). Within the period from 0958 to 1358 UTC on 13 October 2001 and on 15 October 2001, no sensible aerosol optical depths could be derived because of the presence of cirrus, as indicated by the Sun photometer as well as the lidar observations (see Figure 1).

[56] Optical depths of 0.35 at 380 nm and of 0.2 at 1020 nm were observed in the morning hours of 13 October

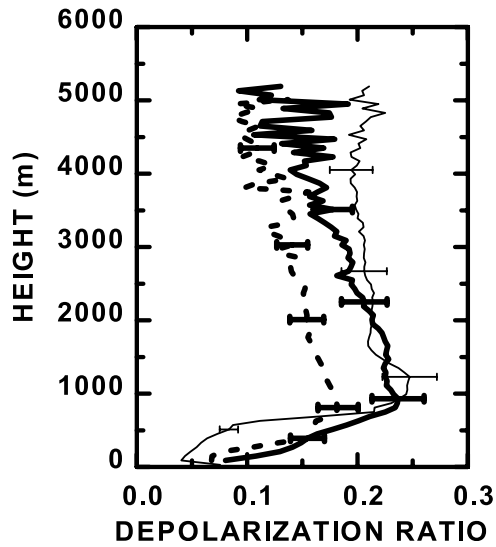

Figure 4. Particle depolarization ratio at 532 nm for the three time frames given in Figure 2. The vertical resolution is 60 m. Meaning of lines is the same as in Figure 2.

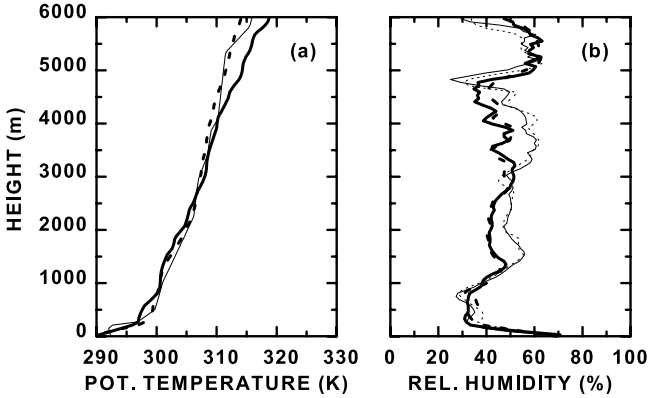

Figure 5. (a) Time series of profiles of potential temperature from radiosonde ascents at 1816 UTC on 13 October 2001 (thin solid line) and at 1200 UTC (dashed solid line) and 1837 UTC (thick solid line) on 14 October 2001. Radiosondes at nighttime were launched at the lidar site. Data at noontime were taken from a radiosonde launched ~50 km northwest of Leipzig. (b) Profiles of relative humidity for the time frames from 1730 to 2007 UTC on 13 October 2001 (thin lines) and from 1738 to 1807 UTC on 14 October 2001 (thick lines). Dotted lines denote profiles from radiosonde. Solid lines denote profiles calculated from radiosonde temperature profiles and the lidar profiles of the water-vapor mixing ratio, respectively.

2001. The optical depth had increased to 0.45 at 380 nm and to 0.35 at 1020 nm during the afternoon. On the following day, 14 October 2001, the optical depth had further increased and peaked at ~0.7 at 380 nm and 0.6 at 1020 nm at noontime. After that, optical depth dropped to ~0.57 at 380 nm and 0.5 at 1020 nm.

[57] The Ångström exponents showed a large variation on 13 October 2001. In the morning hours the exponent was 0.4–0.45. In the afternoon a significant drop to ~0.27 had occurred. On the following day the Ångström exponent was

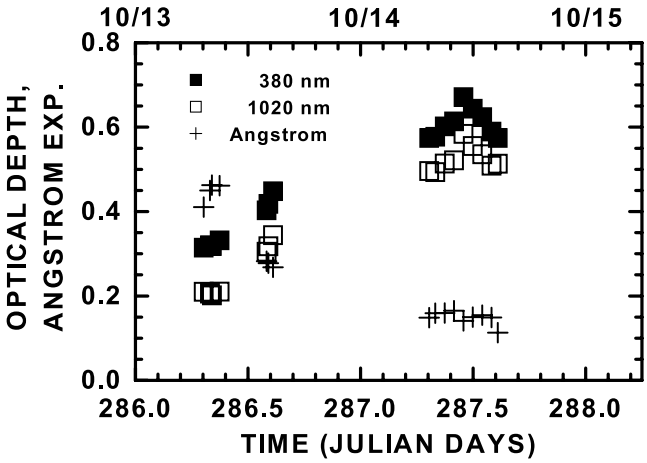

Figure 6. Time series of optical depth at 380 and 1020 nm from Sun photometer observations between 0716 UTC on 13 October 2001 and 1437 UTC on 14 October 2001. Also shown is the time series of the Ångström exponent for the respective wavelength range.

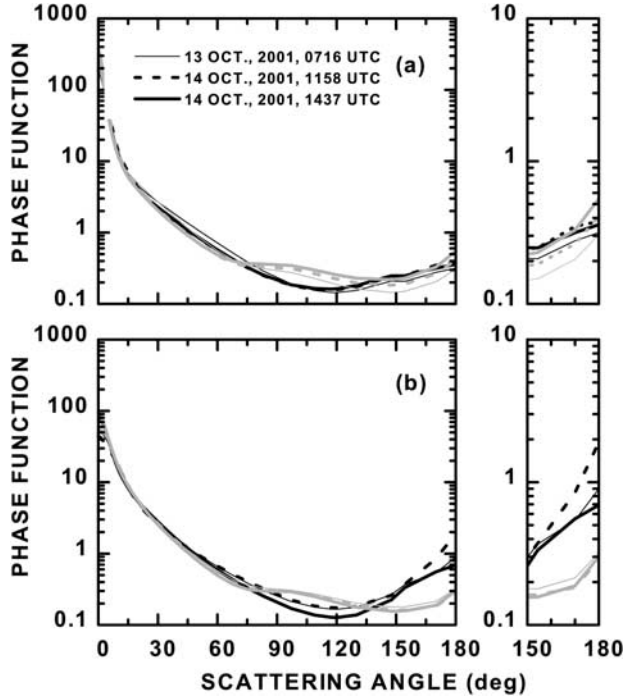

Figure 7. Time series of particle phase function at 440 nm (Figure 7a) and at 1020 nm (Figure 7b) for the spherical particle model (black) and the spheroidal particle model (gray). Respective Sun photometer observations were made at 0716 UTC on 13 October 2001 and at 1158 UTC and at 1437 UTC on 14 October 2001.

almost a factor of 2 less compared to the observations made in the previous afternoon on 13 October 2001. These low values prevailed throughout 14 October 2001. The change toward these low Ångström exponents points to a significant increase of mean particle size in the atmospheric column.

[58] Figure 7 shows the time series of the particle phase functions at 440 nm and at 1020 nm derived from the measurements at 0716 UTC on 13 October 2001 and at 1158 UTC and at 1437 UTC on 14 October 2001. The phase functions were calculated on the basis of the spherical and the spheroidal particle model, respectively.

[59] At both wavelengths the use of the spheroidal model leads to a significant increase of the phase function in the direction of sideward scattering, that is, between ~70° and 130°. There is a strong decrease of the phase function for scattering angles larger than 130°, which is particularly pronounced at the wavelength of 1020 nm. Measurements of sky brightness, which is used for the retrieval of the particle phase functions, were restricted to azimuth angles of <150°. Therefore a direct test of the quality of the retrieved particle phase function in this range of angles could not be done. The average residual error for the sky brightness was ~8.5% for the spherical particle model. The residual error increased in the range of angles from 120° to 150°. In the case of the spheroidal particle model we note a reduction of the average residual error to ~6%. Further, the residual error decreased in the range of angles from 120° to 150°.

[60] For both measurement wavelengths the spheroidal model leads to a reduction of the particle phase function for scattering angles larger than ~130°. This reduction is

particularly pronounced for the measurement wavelength at 1020 nm. The respective phase function at 180° is a factor of $\approx 2-4$ lower in the case of the spheroidal model compared to the spherical model. In the simulations a mixture of oblate and prolate particles with aspect ratios between 1.6 and 2.2 was used, see section 2.2. As pointed out by *Mishchenko et al.* [1997], a nonspherical geometry of the scatterers may be responsible for a strong reduction of the phase function at 180°.

[61] The rather large uncertainty of 50% for the particle phase function in the backward direction as well as the difficulty in deciding which of the two particle models is more appropriate for the description of particle shape becomes obvious if the respective time series are compared with the time series for the particle depolarization ratio. The column-mean depolarization ratio is ~14% for the measurement at noon on 14 October 2001. In contrast the other two periods of lidar observations resulted in a slightly larger column-mean value of ~19% (see Figure 4).

[62] The lower mean depolarization ratio observed around noontime on 14 October 2001 implies that the nonspherical shape of the particles with respect to the measurement wavelength became less important as the result of a smaller mean particle size. Another reason may be that for fixed mean particle size the particles had a more spherical shape. Under consideration of the results presented by *Mishchenko et al.* [1997], both effects should lead to an increase of the particle phase function at 180° compared to the other two observational periods.

[63] As can be seen from Figure 7 the spherical model causes such an increase of the particle phase function at 180° for both measurement wavelengths. However, the spheroidal particle model, which, in fact, should be more appropriate for the description of the conditions, shows a constant increase of the phase function at 440 nm during the course of the three measurement periods. At 1020 nm there is practically no temporal change.

[64] The temporal change of the particle depolarization ratio may be explained as the result of a temporal change of effective radius. For this purpose we used results from respective simulations given in literature [*Mishchenko and Sassen*, 1998], as well as results from the inversion of the Sun photometer data.

[65] *Mishchenko and Sassen* [1998] presented particle depolarization ratios at 532 nm in dependence of particle effective radius and particle asphericity. Particle asphericity was defined in terms of the aspect ratio for prolate and oblate particles. For the present measurements this ratio was not known. Therefore the range of effective radii was determined in dependence of the particle depolarization ratio for the range of aspect ratios from 1.1 to 2.4 [*Mishchenko and Sassen*, 1998]. Further, the investigations were restricted to a simple monomodal power-law distribution [*Mishchenko and Sassen*, 1998]. As outlined in previous studies [*Hansen and Travis*, 1974; *Mishchenko and Travis*, 1994] different kinds of particle size distributions may be well represented by just two parameters, that is, effective radius and effective variance. If particle size distributions of different shape of the distribution are similar for these two parameters, their optical properties are similar as well.

[66] On the basis of a fixed effective variance of 0.1, which corresponds to moderately wide particle size distributions, and a column-mean particle depolarization ratio of 14% we found effective radii from 0.35 to 0.55 μm. Larger depolarization ratios of 19% result in larger effective radii of 0.4–0.75 μm [*Mishchenko and Sassen*, 1998].

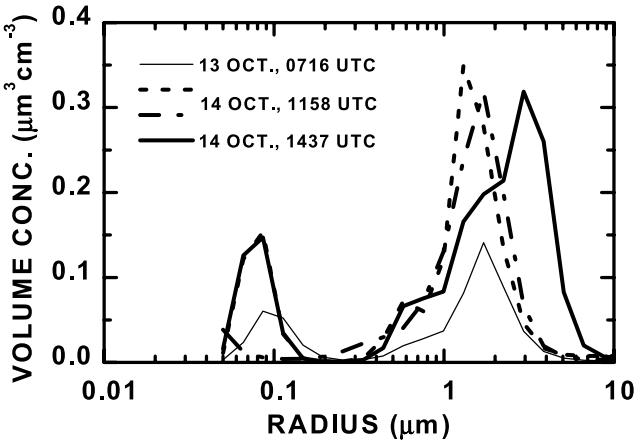

Figure 8. Time series of column-averaged particle size distribution retrieved from the Sun photometer data taken at the times given in Figure 7. Results are shown for the spherical particle model. Also shown is the example retrieved on the basis of the spheroidal particle model for the measurement at 1158 UTC on 14 October 2001 (dash-dotted).

[67] Figure 8 shows examples of particle volume concentration distributions retrieved from the inversion of the Sun photometer data. The shape of the particle concentration distribution shows two modes in the case of the spherical particle model. One reason for the bimodal shape may be the mixture of desert dust and anthropogenic pollution in the boundary layer. However, in part, the pronounced mode at small particle sizes is also caused by the particle geometry and thus the use of the wrong particle model. Figure 8 also shows an example for the particle volume concentration distributions retrieved with the spheroidal particle model for the measurement at noontime on 14 October 2001. The application of the spheroidal particle model significantly decreased the artifacts, which are created in the particle size distribution and the complex refractive index because of the nonspherical geometry of the particles (see section 2.2).

[68] An effective radius of 0.31 μm was retrieved with the spherical particle model for the observation on 13 October 2001. The spheroidal model resulted in a much larger effective radius of 0.73 μm. There was a strong increase of the particle volume concentration on 14 October 2001 compared to the respective concentrations observed in the morning hours on 13 October 2001. The mean size in both modes had shifted toward smaller values during the noontime observations on 14 October 2001. Accordingly, the effective radius was 0.28 μm at that time. This value for the spherical model may be compared to the significantly larger effective radius of 0.59 μm retrieved from the spheroidal model. In both cases the reduction of effective radius may have caused the reduction of the particle depolarization ratio and the increase of the phase function retrieved from the spherical particle model.

Table 1. Microphysical Particle Parameters Derived From the Sun Photometer Data[a]

Date	Time, UTC	r_{eff}, μm	m_{real}	m_{imag}	ω
13 October	0716	0.31 (0.73)	1.41 (1.51)	0.0031 (0.0039)	0.94 (0.93)
14 October	1158	0.28 (0.59)	1.49 (1.56)	0.0026 (0.0026)	0.95 (0.95)
14 October	1437	0.36 (0.58)	1.47 (1.57)	0.0020 (0.0014)	0.95 (0.96)

[a]The parameter r_{eff} denotes the effective radius; m_{real} and m_{imag} are the real part and the imaginary part, respectively, of the complex refractive index. The parameter ω denotes the single-scattering albedo. Numbers for the complex refractive index and the single-scattering albedo are given for the measurement wavelength at 670 nm. First values refer to spherical particle model; numbers in parentheses refer to spheroidal particle model.

[69] The increase of the depolarization ratio in the afternoon on 14 October 2001 may be largely caused by the shift of mean particle size in the coarse mode from 1.33 μm to 1.8 μm. The effective radius of the total size distribution had increased from 0.28 μm to 0.36 μm. These numbers follow from the spherical particle model. From the spheroidal model followed a constant effective radius around 0.59 μm. However, effective radius in the coarse mode increased from 1.4 μm to 1.8 μm. Again in the case of the spherical particle model this increase of effective radius is reflected in the increase of the particle depolarization ratio and the decrease of the phase function at 180°. In contradiction to these observations the spheroidal particle model results in a further increase by ~50% of the particle phase function at 180° at 440 nm. At 1020 nm the phase function remained rather constant. Again this discrepancy may be explained by the rather larger error for the particle phase functions at this angle.

[70] Table 1 summarizes the results for effective radius, complex refractive index, and single-scattering albedo of the particles derived from the inversion of the Sun photometer data. A detailed presentation of the microphysical particle properties of this dust plume will be given in a future contribution. Again the results are given for both particle models used in the retrieval.

[71] In general the derived quantities are characteristic for mineral particles. Effective radii were quite large, in accordance with the rather low Ångström exponents (cf. Figure 6). The real part of the complex refractive index was 1.4–1.6 at 670 nm. The imaginary part of the complex refractive index is 0.0014–0.004 at this wavelength. There is negligible absorption for mineral particles in the visible wavelength range. It has to be pointed out that with decreasing wavelength there was a significant increase of the imaginary part. This enhanced absorption in the ultraviolet part of the electromagnetic spectrum agrees well with results given elsewhere [*Patterson et al.*, 1977; *d'Almeida et al.*, 1991]. The single-scattering albedo was 0.93–0.96.

4. Discussion

4.1. Comparison of Optical Depth

[72] Figure 9 shows the time series of optical depth at 532 nm on the basis of the Sun photometer and the lidar observations from 0716 UTC on 13 October 2001 until 1807 UTC on 14 October 2001. The Sun photometer measurements were interpolated to the wavelength of 532 nm by a linear fit between the data at 500 and 670 nm. In the case of the lidar observations we present total columnar optical depth, the contribution by the dust layer above 1000-m height and the layer below 1000-m height.

[73] Optical depth increased from 0.39 to 0.47–0.49 within the 3 hours between the last Sun photometer measurement on 13 October 2001 and the nighttime measurement with lidar. The lower value of optical depth from lidar follows from a lidar ratio of 40 sr below 1000-m height, whereas the upper value follows under the assumption of a lidar ratio of 60 sr. According to the lidar observations the dust layer above 1000-m height contributed 86%–89% to total optical depth. Within the ranges of uncertainty given by the measurements and the modelling uncertainties there is excellent agreement of optical depth derived from the extinction profiles to optical depth derived from Sun photometer for the time frame from 1151 to 1323 UTC on 14 October 2001. Optical depth from lidar is 0.08–0.12 in the boundary layer. Lower and upper values again follow from the assumption of a lidar ratio of 40 sr and 60 sr, respectively. Optical depth below 1000-m height is ~0.1 if it is calculated as the difference between optical depth determined with Sun photometer and optical depth above 1000-m height determined with lidar. This value converts into a lidar ratio of 50 sr for the respective height range. Eighty percent to eighty-six percent of the columnar optical depth was contributed by the Saharan dust layer above 1000-m height. Finally, the lidar measurement between 1737 and 1807 UTC on 14 October 2001 again shows a contribution

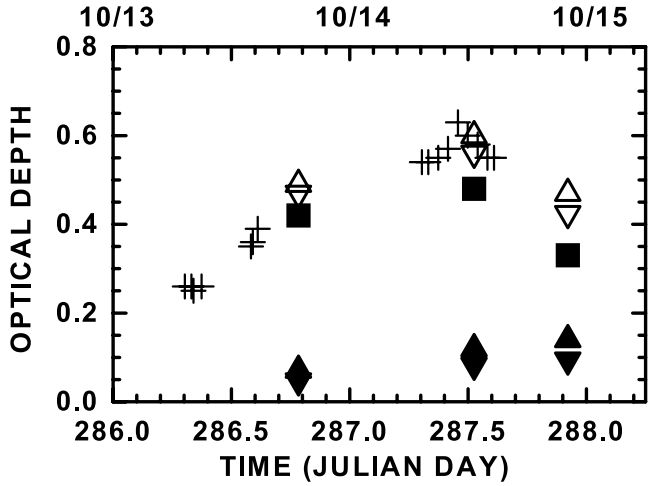

Figure 9. Time series of optical depth at 532 nm (crosses). The Sun photometer values were obtained through linear interpolation between the values at 500 and 670 nm. The time frame is the same as in Figure 6. Also shown are optical depths from lidar, that is, optical depth above 1000-m height (closed squares), optical depth below 1000-m height under assumption of lidar ratio of 40 sr (downward pointing closed triangles), optical depth below 1000-m height under assumption of lidar ratio of 60 sr (upward pointing closed triangles), and respective total optical depth (upward and downward pointing open triangles). The time frame for which the lidar values are given is the same as in Figure 2.

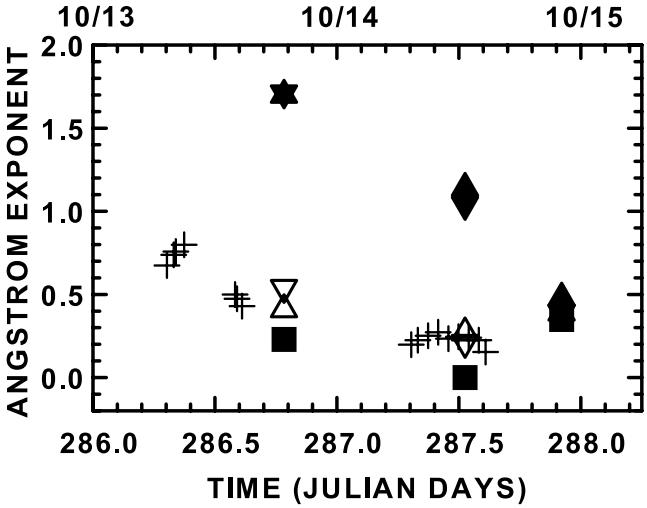

Figure 10. Time series of Ångström exponents based on Sun photometer observations at 380 and 670 nm and lidar observations at 355 and 532 nm. Meaning of symbols is the same as in Figure 9.

of 70%–78% of the dust layer to total columnar depth, which was 0.42–0.47.

4.2. Comparison of Ångström Exponents

[74] Figure 10 shows the comparison of Sun photometer and lidar observations in terms of column-averaged Ångström exponents. The time series for Sun photometer is based on observations of optical depth at 380 and 670 nm. The Ångström exponents on the basis of the lidar observations are given as column-averaged values, and the individual contributions above 1000-m height and below 1000-m height. These values follow from the profiles of the Ångström exponents presented in Figure 2c.

[75] Ångström exponents from the Sun photometer observations are 0.68–0.8 in the morning hours of 13 October 2001. The afternoon observations show a drop to 0.43–0.5. Comparably low column-averaged Ångström exponents of 0.41–0.54 were found from the following nighttime observation. The average value in the dust plume above 1000-m height was 0.23. The mean Ångström exponent was 1.7 below 1000-m height.

[76] Considerably lower Ångström exponents of 0.25 on the basis of Sun photometer observations were seen on 14 October 2001. For the time period from 1151 to 1323 UTC we find excellent agreement to the column-averaged value of 0.21–0.27 from lidar.

[77] The Ångström exponent below 1000-m height was also determined from optical depth calculated as the difference between total optical depth from Sun photometer and optical depth above 1000-m height from lidar. In this case the Ångström exponent of 0.96 deviates <15% from the lidar-derived value of 1.04–1.14.

[78] The nighttime observations on 14 October 2001 result in a column-averaged Ångström exponent of 0.39. This rather large Ångström exponent, compared to the observations at noon, indicates the end of the dust outbreak. The mean Ångström exponent in the dust layer above 1000-m height was 0.35. The Ångström exponent within the boundary layer was 0.39–0.48 and thus almost as low as in the dust plume. For comparison at noontime the Ångström exponent in this height range was approximately one. We conclude that the planetary boundary layer showed a comparably high concentration of dust particles during the nighttime observation.

4.3. Comparison of Lidar Ratio

[79] Figure 11 shows the comparison of the lidar ratio at 532 nm from the lidar observations (see Figure 2) with the column-averaged value from Sun photometer for the observational period from 1151 to 1327 UTC on 14 October 2001. The lidar ratio from Sun photometer was determined according to equations (3)–(5). A column averaged lidar ratio of 62 ± 12 sr follows from the lidar data. The column-averaged lidar ratio from Sun photometer is ~29 ± 15 sr for the spherical particle model. The use of the spheroidal model gives a slightly larger lidar ratio of 35 ± 18 sr.

[80] Errors of single-scattering albedo and optical depth, which enter the calculation of the lidar ratio in the case of the Sun photometer data in summary are ~5% and thus of minor importance. Further, optical depth from lidar agreed very well with the respective value from Sun photometer, see Figure 7. The particle phase function at 180°, however, may be affected by errors as large as 50% (see section 2.2).

[81] Even under consideration of these errors there is no agreement between the lidar ratio measured with lidar and the lidar ratio calculated on the basis of the spherical particle

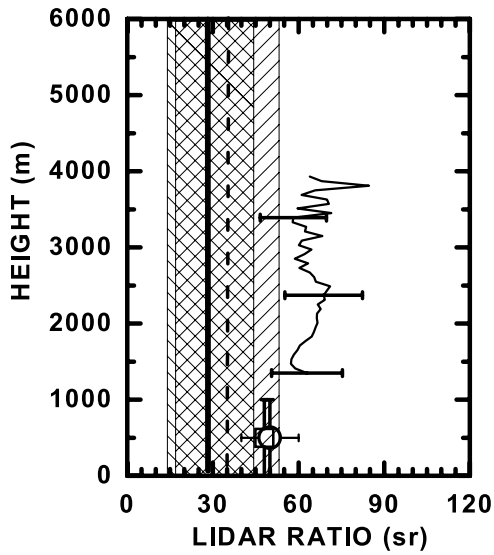

Figure 11. Profile of the particle lidar ratio at 532 nm on the basis of lidar observations from 1151 to 1323 UTC on 14 October 2001. Error bars are given as horizontal lines. From 0 to 1000-m height a column-averaged value is given. It follows in combination with optical depth from Sun photometer observations (square). Lidar ratios of 40 and 60 sr, which were assumed below 1000-m height, are shown for comparison (open circle and error bar). Thick solid line denotes the column-averaged lidar ratio estimated from Sun photometer with the spherical particle model. Shaded area (lines to the left) denotes uncertainty. Thick dashed line denotes the column-averaged lidar ratio estimated from Sun photometer with the spheroidal particle model. Shaded area (lines to the right) denotes uncertainty.

model. In the case of the spheroidal model the lidar ratio is at the lower limit given by the value derived with lidar. The value for the phase function at 180° has to be decreased further by a factor of almost 2 in order to obtain the mean lidar ratio from the lidar measurements. Future work will focus on the improvement of the spheroidal particle model. The distribution of the aspect ratios has to be modified in such a way that the lidar ratios calculated with this new model match the lidar observations. An example of such an approach in the case of desert dust from Asia has been given only recently [*Liu et al.*, 2002].

[82] As outlined by *Mattis et al.* [2002b], the observed lidar ratios at 532 nm are rather large. Only few numbers for comparison can be found in literature. Large values of 40–75 sr at 532 nm on the basis of measurements with Raman lidar and high-spectral-resolution lidar have been reported for yellow dust outbreaks observed over Japan [*Murayama et al.*, 2001; *Liu et al.*, 2002]. Lidar ratios of 15–62 sr at 600 nm were found for Saharan dust over Barbados [*Sasano and Browell*, 1989]. These lidar ratios were estimated from simple backscatter lidar observations and thus have to be used with caution (cf. section 2.1). Lidar ratios of 40 sr at 532 nm were found for Saharan dust observed over the island of Tenerife (Canary Islands) off the west coast of North Africa [*Welton et al.*, 2000]. Here as well, the lidar ratio was estimated on the basis of backscatter lidar observations with optical depths from Sun photometer observations serving as constraining information. A lidar ratio of 35 ± 5 sr at 532 nm was found from respective slant-path lidar observations [*Powell et al.*, 2000]. Lidar ratios in the range from 25 to 35 sr at 532 nm were assumed for Saharan dust observed during the Lidar In-space Technology Experiment (LITE) over the eastern Atlantic region [*Karyampudi et al.*, 1999]. A range of values from 49 to 87 sr at 500 nm was estimated for Asian dust events on the basis of observations with polar nephelometer [*Nakajima et al.*, 1989]. However, this instrument could not provide direct measurements of phase functions at 180° and single-scattering albedo. The parameters were constructed on the basis of a semiempirical theory for irregular particles [*Pollack and Cuzzi*, 1980]. Slant-path lidar observations in the arid southwest of the United States yielded lidar ratios between 10 and 45 sr at 694 nm [*Reagan et al.*, 1988]. Herein, values in the range between 10 and 20 sr were attributed to soil-type, almost nonabsorbing particles in the coarse mode. Finally, Mie-scattering calculations with typical size distributions of desert dust yielded lidar ratios in the range of 15–30 sr [*Ackermann*, 1998; *Barnaba and Gobbi*, 2001].

[83] Two effects may be responsible for the large lidar ratios reported here. During the transport from the source regions to the lidar site a large amount of coarse-mode particles above 1 μm in diameter may have been removed by sedimentation. For comparison, effective radii from the inversion of the Sun photometer data were 0.28–0.73 μm (see Table 1). Effective radii from 0.28 to 0.55 μm were estimated on the basis of the theoretical investigations made by *Mishchenko and Sassen* [1998] (see section 3.2). Simulations have shown that lidar ratios increase if particle size decreases [*Mishchenko et al.*, 1997; *Ackermann*, 1998; *Barnaba and Gobbi*, 2001; *Franke et al.*, 2001; *Liu et al.*, 2002].

[84] The most important reason responsible for the large lidar ratios is believed to be the nonspherical shape of the scatterers, which causes the reduction of the particle backscatter coefficient. According to *Mattis et al.* [2002b], the lidar ratio at 532 nm should be reduced by a factor of 1.5–3 if transformed to the respective values for spherical equivalent particles of the same geometrical surface. This estimate followed from correction factors given by *Mishchenko et al.* [1997].

[85] Only recently *Kalashnikova and Sokolik* [2002] have shown that the particle phase function at 180° may be reduced by one order of magnitude compared with the respective value for surface-equivalent spheres. In their calculations, which were done for the wavelength of 550 nm, the authors assumed for example sharp-edged particles, which probably present a better approximation for the shape of natural dust particles than the ellipsoidal shapes assumed by *Mishchenko et al.* [1997].

[86] In this presentation we continued the analysis of the correction of the lidar ratio through comparison of the measured extinction spectra to the respective properties obtained from Mie-scattering calculations [*Bohren and Huffman*, 1983]. The calculated lidar ratios for which the respective extinction coefficients match the measured extinction spectra should provide the correction factor that describes the influence of the nonspherical geometry of the particles on the backscatter coefficients. The lidar ratios derived from the Sun photometer observations with the two models for particle shape also were tested against this correction factor. In contrast to the simple comparison on the basis of the Mie-scattering calculations the results from the Sun photometer data contain the additional information of the particle phase function.

[87] In order to achieve a statistically significant result on the basis of synthetic data a large amount of Mie spectra has to be considered. To account for the shape and the modality of the size distributions in the Mie-scattering calculations thus requires an enormous computational effort. The situation is complicated by the fact that the inversion results from Sun photometer showed a bimodal shape of the particle size distribution. Even in the simple case that only one specific shape of the size distribution is chosen, for example, a logarithmic-normal shape, it still would leave us with six parameters for the size distribution. However, as outlined in section 3.2, effective radius and effective variance control the results irrespective of the specific shape of the particle size distribution [*Hansen and Travis*, 1974; *Mishchenko and Travis*, 1994]. The calculations, therefore, were restricted to monomodal logarithmic-normal distributions leaving us with three parameters for the size distribution.

[88] For the particle size distributions we chose mode radii from 0.02 to 0.1 μm in steps of 0.01 μm and from 0.1 to 0.4 μm in steps of 0.05 μm. Mode widths were between 1.4 and 2.5 with a stepwidth of 0.1. Only those particle size distributions were used, for which effective radii were between 0.2 and 1 μm. Effective variance for the chosen particle size distributions was between 0.12 and 1.3. The particles sizes include the range of numbers provided in literature [e.g., *d'Almeida et al.*, 1991]. The particle sizes also cover the results for mean particle size obtained from the analysis of the particle depolarization ratio (cf. section

3.2), and the results for the microphysical particle properties obtained from the inversion of the Sun photometer data (cf. Table 1).

[89] Complex refractive indices were chosen wavelength independent and in the range provided in literature [*Patterson et al.*, 1977; *Arao and Ishizaka*, 1986; *d'Almeida et al.*, 1991; *Ackermann*, 1998]; that is, real parts were 1.4–1.6 in steps of 0.025. These real parts cover the real part obtained from the inversion of the Sun photometer data. The inversion under assumption of the spherical particle model delivered an unrealistically low real part of 1.33 at 440 nm, which therefore was not considered in the present study. The imaginary part at 532 nm took values of 0.001, 0.0025, 0.005, and 0.0075. For comparison, imaginary parts from the inversion were 0.0025–0.0043 in this wavelength range. Mineral particles show increased light absorption in the ultraviolet wavelength range [*d'Almeida et al.*, 1991]. Therefore the imaginary part at 355 nm was set to 0.0125, 0.015, 0.0175, and 0.02. Approximately 200,000 different extinction spectra were considered in this search.

[90] Input for the search algorithm was the column-averaged Ångström exponent derived from the extinction profiles at 355 and 532 nm (see Figure 2). Its value was set to 0.24 ± 0.07, which was found for the atmospheric column at noontime on 14 October 2001. The uncertainty of 0.07 takes account of the uncertainty of the extinction profiles at 355 and 532 nm, and the uncertainty of the lidar ratio below 1000-m height. At noontime the minimum value of the column-averaged Ångström exponent and the maximum of optical depth was reached. The influence of small particles from anthropogenic pollution within the boundary layer should be negligibly low. A comparably large Ångström exponent of 0.23 was found for the dust plume above 1000-m height in the nighttime measurement on 13 October 2001.

[91] Figure 12 presents the results of the search of the Mie spectra with respect to the lidar ratio at 532 nm. 2170 out of the 200,000 extinction spectra were found to be consistent with the imposed constraints, which included effective radii from 0.2 to 1 μm. Consideration of the reduced range of effective radii from 0.2 to 0.6 μm (cf. Table 1) resulted in 1571 solutions, which are shown in Figure 12. The extended solution set did not show significant differences. The shape of the distribution function shown in Figure 12 was almost the same, only the absolute values were a little larger.

[92] Solutions were found in the range from 8 to 98 sr. However, the number of solutions was not equally distributed across the solution space. The maximum of individual solutions was roughly at 21 sr. Upper and lower lidar ratio at half maximum was ~34 and 14 sr, respectively. Fifty percent of all solutions were between 8 and 34 sr. For comparison the lidar ratio of 29 sr from the spherical particle model is rather close to the maximum of the distribution function.

[93] According to Figure 12 the correction factor is in the range from 0.23–0.56; that is, the lidar ratio has to be multiplied by a factor of 1.8–4.4. These numbers hold for the range of lidar ratios at half maximum, that is, from 14–34 sr. A multiplication factor of 2.2 follows from the results obtained with the Sun photometer measurements on the basis of the spherical particle model. As pointed out before the results from Sun photometer include information of optical depth and particle phase function. Therefore a deviation of the correction factor from the simple comparison of Mie spectra has to be expected. The results shown in Figure 12 are representative for the range of lidar ratios usually found for spherical scatterers [*Ackermann*, 1998; *Barnaba and Gobbi*, 2001]. The present study for the first time provided the link to measured lidar ratios of particles of nonspherical geometry from the Saharan source regions.

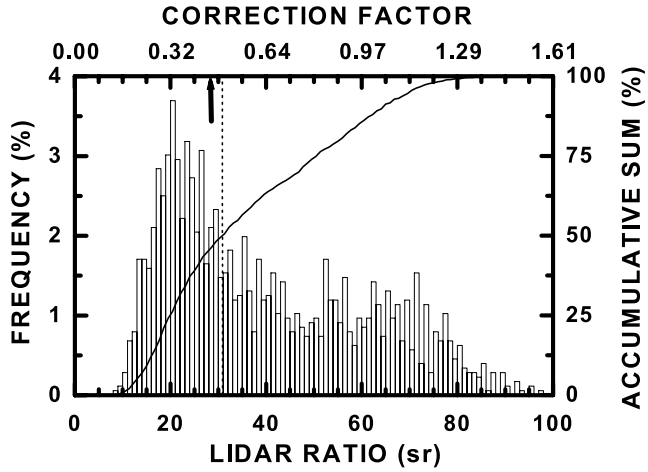

Figure 12. Histogram distribution of individual solutions for particle lidar ratio at 532 nm. Length of bars denote the percentage of individual solutions to total number of solutions. Stepwidth of bars is 1 sr. Trace denotes accumulative distribution of individual solutions. Fifty percent of all solutions are found below 32 sr (vertical line). The arrow denotes the correction factor that follows from the Sun photometer data with the spherical particle model.

[94] It is interesting to note that effective variance was in the range from 0.12 to 1.15. Seventy percent of all solutions were between 0.41 and 1.15. The range for effective variance is considerably larger than the respective numbers of 0.1–0.4 considered by *Mishchenko et al.* [1997]. In their studies a power-law distribution was used. The maximum geometrical mean radius used in their simulations was ~0.45 μm, and thus well within the range of 0.2–0.6 μm used in our study. The discrepancy with respect to effective variance may be largely explained by the different range of particle size. *Mishchenko et al.* [1997] only considered particles with a maximum size of 2 μm. This cut-off at rather small particle sizes was compensated for by a rather narrow particle size distribution in order to come up with a mean particle size of 0.45 μm, which is a reasonable value in the case of desert dust. For example, an effective variance of 0.4 is equivalent to 1.6 in standard deviation for a monomodal logarithmic-normal distribution. For comparison, we used maximum standard deviations of up to 2.5. Values of 1.6–2.5 are given in literature for particle size distributions of mineral and dust-like material [*d'Almeida et al.*, 1991].

5. Summary

[95] We have presented for the first time a comprehensive characterization of optical properties of a Saharan dust

outbreak over central Europe on the basis of a combined study with an advanced aerosol Raman lidar and a Sun photometer. The lidar is part of the European Aerosol Research Lidar Network (EARLINET). The Sun photometer is part of the Aerosol Robotic Network (AERONET) operated by NASA. The outbreak occurred from 12 to 15 October 2001 and was observed by most of the other EARLINET stations.

[96] The plume reached from near surface to a maximum height of 6000 m. According to backward trajectories the source region of the plumes was in the western regions of the Sahara. Maximum optical depths of 0.67 at 380 nm and of 0.58 at 1020 nm were observed with Sun photometer around noon on 14 October 2001. Concurrent lidar observations throughout the dust period showed that up to 90% of optical depth was contributed by the dust layer above 1000-m height. Ångström exponents describing extinction in the wavelength range from 380 to 670 nm were 0.2 during the peak of the dust outbreak. Ångström exponents in the center of the dust plume were as low as −0.2. These numbers point to large particles in the dust plume. Lidar profiles showed large mean Ångström exponents of ∼1.7 below 1000-m height on 13 October 2001. The presence of mineral particles in the boundary layer on 14 October 2001 lead to a decrease of the Ångström exponents to values as low as 0.39.

[97] Particle depolarization ratios showed very large values between 20% and 25% at 532 nm on 13 October 2001 and during the nighttime observations on 14 October 2001. There was a significant drop toward lower values of 10%–20% during the peak of the dust outbreak at noon on 14 October 2001. The particle phase function at 180° retrieved from the Sun photometer data with the spherical particle model used in this study increased around noontime on 14 October 2001. On the basis of theoretical models of nonspherical particles and the inversion of the Sun photometer data it was concluded that mean particle size had dropped by ∼20% during the peak period of the dust event, and thus could explain the observed temporal change of the particle depolarization ratio. Slightly contradictory results were obtained from the second particle model used in this study, which describes particles as spheroids. This result is mainly caused by the large uncertainties involved in the retrieval of the particle phase functions.

[98] Absolutely cloud-free conditions around noontime on 14 October 2001 allowed a direct comparison of optical depths, Ångström exponents, and lidar ratios derived from both instruments. A rigorous test of the assumptions made in the retrieval procedures for both instruments resulted in an excellent agreement of particle optical depth and Ångström exponents. The mean value of optical depth derived from lidar was ∼0.58 at 532 nm. The Sun photometer observations resulted in a mean optical depth of 0.6. The mean Ångström exponent from lidar was 0.21–0.27, whereas the Sun photometer gave a mean value of 0.24.

[99] There was substantial deviation between the lidar ratios obtained from both instruments. It was explained by the nonspherical shape of the scatterers. This nonspherical geometry of the particles causes a reduction of the backscatter phase function and thus may be responsible for the large lidar ratios of 50–80 sr at 532 nm observed in the center of the dust plume above 1000-m height. The column-averaged lidar ratio at noontime on 14 October 2001 was 62 ± 12 sr. For comparison, the Sun photometer observations resulted in a column-averaged lidar ratio of 29 ± 15 sr if the spherical particle model was used. This comparison suggests a reduction of the lidar ratio by a factor of 2.2 if the observed particles are treated as surface-equivalent spherical scatterers. A sensitivity analysis on the basis of Mie-scattering calculation confirmed this reduction.

[100] Contradictory results were obtained if the spheroidal particle model was used for the calculation of the lidar ratio. The value of 35 ± 18 sr is considerably lower than the value obtained with lidar. The deviation suggests that some of the assumptions made for the model of spheroidal particles did not appropriately describe the particle properties. On the other hand the knowledge of the correct lidar ratio could allow for a respective correction of the spheroidal particle model by choosing that aspect ratio for the spheroidal particles for which the derived lidar ratio matches the measured value.

[101] **Acknowledgments.** The EARLINET project is funded by the European Commission, Grant No. EVR1-CT-1999-40003. We wish to express our gratitude to Brent Holben for providing the Sun photometer data.

References

Ackermann, J., The extinction-to-backscatter ratio of tropospheric aerosol: A numerical study, *J. Atmos. Oceanic Technol.*, *15*, 1043–1050, 1998.

Ångström, A., The parameters of atmospheric turbidity, *Tellus*, *16*, 64–75, 1964.

Ansmann, A., M. Riebesell, and C. Weitkamp, Measurements of atmospheric aerosol extinction profiles with a Raman lidar, *Opt. Lett.*, *15*, 746–748, 1990.

Ansmann, A., U. Wandinger, M. Riebesell, C. Weitkamp, E. Voss, W. Lahmann, and W. Michaelis, Combined Raman elastic-backscatter lidar for vertical profiling of moisture, aerosols extinction, backscatter, and lidar ratio, *Appl. Phys. B*, *55*, 18–28, 1992a.

Ansmann, A., U. Wandinger, M. Riebesell, C. Weitkamp, and W. Michaelis, Independent measurement of extinction and backscatter profiles in cirrus clouds by using a combined Raman elastic-backscatter lidar, *Appl. Opt.*, *31*, 7113–7131, 1992b.

Ansmann, A., F. Wagner, D. Müller, D. Althausen, A. Herber, W. von Hoyningen-Huene, and U. Wandinger, European pollution outbreaks during ACE 2: Optical particle properties inferred from multiwavelength lidar and star-Sun photometry, *J. Geophys. Res.*, *107*, 4259, doi:10.1029/2001JD001109, 2002.

Arao, K., and Y. Ishizaka, Volume and mass of yellow sand dust in the air over Japan as estimated from atmospheric turbidity, *J. Meteorol. Soc. Jpn.*, *64*, 79–94, 1986.

Arshinov, Y. F., S. M. Bobrovnikov, V. E. Zuev, and V. M. Mitev, Atmospheric temperature measurements using pure rotational Raman lidar, *Appl. Opt.*, *22*, 2984–2990, 1983.

Arshinov, Y., and S. Bobrovnikov, Use of a Fabry-Perot interferometer to isolate pure rotational Raman spectra of diatomic molecules, *Appl. Opt.*, *38*, 4635–4638, 1999.

Arshinov, Y., S. Bobrovnikov, I. Serikov, D. Althausen, I. Mattis, U. Wandinger, A. Ansmann, Spectrally absolute instrumental approach to isolate pure rotational Raman lidar returns from nitrogen molecules of the atmosphere, in *Laser Remote Sensing of the Atmosphere, Selected Papers of the 20th International Laser Radar Conference, Vichy, France*, edited by A. Dabas, C. Loth, and J. Pelon, pp. 121–124, École Polytechnique, Paris, France, 2001.

Barnaba, F., and G. P. Gobbi, Lidar estimation of tropospheric aerosol extinction, surface area and volume: Maritime and desert-dust cases, *J. Geophys. Res.*, *106*, 3005–3018, 2001.

Bobrovnikov, S. M., Y. F. Arshinov, I. B. Serikov, D. Althausen, A. Ansmann, I. Mattis, U. Wandinger, in *Laser Remote Sensing in Atmosphere and Earth Sciences, Proceedings of the 21st International Laser Radar Conference, Québec City, Canada*, edited by L. R. Bisonette, G. Roy, and G. Vallée, pp. 717–720, Library Services, Defence R&D Canada, Valcartier, Canada, 2002.

Bohren, C. F., and D. R. Huffman, *Absorption and Scattering of Light by Small Particles*, 530 pp., John Wiley, New York, 1983.

Bösenberg, J., et al., EARLINET: A European Aerosol Research Lidar Network, in *Laser remote sensing of the atmosphere. Selected papers of the 20th International Laser Radar Conference, Vichy, France*, edited by A. Dabas, C. Loth, and J. Pelon, pp. 155–158, École Polytechnique, Paris France, 2001.

Cairo, F., G. Di Donfrancesco, A. Adriani, P. Lucio, and F. Federico, Comparison of various linear depolarization parameters measured by lidar, *Appl. Opt.*, *38*, 4425–4432, 1999.

Cooney, J., J. Orr, and C. Tomasettis, Measurements separating the gaseous and aerosol components of laser atmospheric backscatter, *Nature*, *224*, 1098–1099, 1969.

Cooney, J., Comparison of water vapor profiles obtained by radiosonde and laser backscatter, *J. Appl. Meteorol.*, *10*, 301, 1970.

d'Almeida, G. A., P. Koepke, and E. P. Shettle (Eds.), *Atmospheric Aerosols, Global Climatology and Radiative Characteristics*, 561 pp., A. Deepak, Hampton, Va., 1991.

Di Sarra, A., T. di Iori, M. Cacciani, G. Fiocco, and D. Fua, Saharan dust profiles measured by lidar at Lampedusa, *J. Geophys. Res.*, *106*, 10,335–10,348, 2001.

Dubovik, O., and M. D. King, A flexible inversion algorithm for retrieval of aerosol optical properties from Sun and sky radiance measurements, *J. Geophys. Res.*, *105*, 20,673–20,696, 2000.

Dubovik, O., A. Smirnov, B. N. Holben, M. D. King, Y. J. Kaufman, T. F. Eck, and I. Slutsker, Accuracy assessments of aerosol optical properties retrieved from Aerosol Robotic Network (AERONET) Sun and sky radiance measurements, *J. Geophys. Res.*, *105*, 9791–9806, 2000.

Dubovik, O., B. N. Holben, T. F. Eck, A. Smirnov, Y. J. Kaufman, M. D. King, and I. Slutsker, Variability of absorption and optical properties of key aerosol types observed in worldwide locations, *J. Atmos. Sci.*, *59*, 590–608, 2002a.

Dubovik, O., B. N. Holben, T. Lapyonok, A. Sinyuk, M. I. Mishchenko, P. Yang, and I. Slutsker, Non-spherical aerosol retrieval method employing light scattering by spheroids, *Geophys. Res. Lett.*, *29*, 1415, 10.1029/2001GL014506, 2002b.

European Centre for Medium-Range Weather Forecasts (ECMWF), User guide to ECMWF products 2.1, *Meteorol. Bull. M3.2*, Reading, England, 1995.

Evans, B. T. N., Sensitivity of the backscatter/extinction ratio to changes in aerosol properties: implication for lidar, *Appl. Opt.*, *27*, 3299–3305, 1988.

Fernald, F. G., Analysis of atmospheric lidar observations: Some comments, *Appl. Opt.*, *23*, 652–653, 1984.

Ferrare, R. A., S. H. Melfi, D. N. Whiteman, K. D. Evans, R. Leifer, and Y. J. Kaufman, Raman lidar measurements of aerosol extinction and backscattering, Part 1, Methods and comparisons, *J. Geophys. Res.*, *103*, 19,663–19,672, 1998.

Franke, K., A. Ansmann, D. Müller, D. Althausen, F. Wagner, and R. Scheele, One-year observations of particle lidar ratio over the tropical Indian Ocean with Raman lidar, *Geophys. Res. Lett.*, *28*, 4559–4562, 2001.

Gobbi, G. P., F. Barnaba, R. Giorgi, and A. Santacasa, Altitude-resolved properties of a Saharan dust event over the Mediterranean, *Atmos. Environ.*, *34*, 5119–5127, 2000.

Hamonou, E., P. Chazette, D. Balis, F. Dulac, X. Schneider, E. Galani, G. Ancellet, and A. Papayannis, Characterization of the vertical structure of Saharan dust export to the Mediterranean basin, *J. Geophys. Res.*, *104*, 22,275–22,270, 1999.

Hansen, J. E., and L. D. Travis, Light scattering in planetary atmospheres, *Space Sci. Rev.*, *16*, 527–610, 1974.

Haywood, J. M., P. N. Francis, M. D. Glew, and J. P. Taylor, Optical properties and direct radiative effect of Saharan dust: A case study of two Saharan dust outbreaks using aircraft data, *J. Geophys. Res.*, *106*, 18,417–18,430, 2001.

Holben, B. N., et al., AERONET - A federated instrument network and data archive for aerosol characterization, *Remote Sens. Environ.*, *66*, 1–16, 1998.

Holben, B. N., et al., An emerging ground-based aerosol climatology: Aerosol optical depth from AERONET, *J. Geophys. Res.*, *106*, 12,067–12,097, 2001.

Intergovernmental Panel on Climate Change (IPCC), *Climate Change 2001: The Scientific Basis*, edited by J. T. Houghton et al., Cambridge Univ. Press, New York, 2001.

Kalashnikova, O. V., and I. N. Sokolik, Importance of shapes and compositions of wind-blown dust particles for remote sensing at solar wavelengths, *Geophys. Res. Lett.*, *29*, 1398, doi:10.1029/2002GL014947, 2002.

Karyampudi, V. M., S. P. Palm, J. A. Reagan, H. Fang, W. B. Grant, R. M. Hoff, C. Moulin, H. F. Pierce, O. Torres, E. V. Browell, and S. H. Melfi, Validation of the Saharan dust plume conceptual model using lidar, Meteosat, and ECMWF data, *Bull. Am. Meteorol. Soc.*, *80*, 1045–1075, 1999.

Klett, J. D., Stable analytical inversion solution for processing lidar returns, *Appl. Opt.*, *20*, 211–220, 1981.

Li, X., H. Maring, D. Savoie, K. Voss, and J. M. Prospero, Dominance of mineral dust in aerosol light scattering in the North Atlantic trade winds, *Nature*, *380*, 416–419, 1996.

Liu, Z., N. Sugimoto, and T. Murayama, Extinction-to-backscatter ratio of Asian dust observed with high-spectral-resolution lidar and Raman lidar, *Appl. Opt.*, *41*, 2760–2767, 2002.

Masonis, S. J., K. Franke, A. Ansmann, D. Müller, D. Althausen, J. A. Ogren, A. Jefferson, and P. J. Sheridan, An intercomparison of aerosol light extinction and 180° backscatter as derived using in situ instruments and Raman lidar during the INDOEX field campaign, *J. Geophys. Res.*, *107*, 8014, doi:10.1029/2000JD000035, 2002.

Mattis, I., Aufbau eines Feuchte-Temperatur-Aerosol-Ramanlidars und Methodenentwicklung zur kombinierten Analyse von Trajektorien und Aerosolprofilen (Construction of a humidity-temperature-aerosol Raman lidar and development of methods for the combined analysis of trajectories and aerosol profiles), 134 pp., Ph.D. thesis, Univ. Leipzig, Germany, 2002.

Mattis, I., A. Ansmann, D. Althausen, V. Jaenisch, U. Wandinger, D. Müller, Y. F. Arshinov, S. M. Bobrovnikov, and I. B. Serikov, Relative humidity profiling in the troposphere with a Raman lidar, *Appl. Opt.*, *41*, 6451–6462, 2002a.

Mattis, I., A. Ansmann, D. Müller, U. Wandinger, and D. Althausen, Dual-wavelength Raman lidar observations of the extinction-to-backscatter ratio of Saharan dust, *Geophys. Res. Lett.*, *29*, 1306, doi:10.1029/2002GL014721, 2002b.

Melfi, S. H., Remote measurements of the atmosphere using Raman scattering, *Appl. Opt.*, *11*, 1605–1610, 1972.

Melfi, S. H., J. D. Lawrence, and M. P. McCormick, Observation of Raman scattering by water vapor in the atmosphere, *Appl. Phys. Lett.*, *15*, 295–297, 1969.

Mishchenko, M. I., and L. D. Travis, Light scattering by polydispersions of randomly oriented spheroids with sizes comparable to wavelengths of observation, *Appl. Opt.*, *33*, 7206–7225, 1994.

Mishchenko, M. I., L. D. Travis, R. A. Kahn, and R. A. West, Modeling phase functions for dustlike tropospheric aerosols using a shape mixture of randomly oriented polydisperse spheroids, *J. Geophys. Res.*, *102*, 16,831–16,847, 1997.

Mishchenko, M. I., and K. Sassen, Depolarization of lidar returns by small ice particles: An application to contrails, *Geophys. Res. Lett.*, *25*, 309–312, 1998.

Moulin, C., F. Dulac, C. E. Lambert, P. Chazette, I. Jankowiak, B. Chatenet, and F. Lavern, Long-term daily monitoring of Saharan dust load over ocean using Meteosat ISCCP-B2 data, 2, Accuracy of the method and validation of Sun photometer measurements, *Geophys. Res. Lett.*, *102*, 16,595–16,969, 1997.

Müller, D., A. Ansmann, F. Wagner, D. Althausen, K. Franke, and D. Althausen, European pollution outbreaks during ACE 2: Microphysical particle properties and single-scattering albedo inferred from mutliwavelength lidar observations, *J. Geophys. Res.*, *107*, 4248, doi:10.1029/2001JD001110, 2002.

Murayama, T., H. Okamoto, N. Kaneyasu, H. Kamataki, and K. Miura, Application of lidar depolarization measurement in the atmospheric boundary layer: Effects of dust and sea-salt particles, *J. Geophys. Res.*, *104*, 31,781–31,792, 1999.

Murayama, T., et al., Ground-based network observation of Asian dust events of April 1998 in east Asia, *J. Geophys. Res.*, *106*, 18,345–18,359, 2001.

Nakajima, T., and M. Tanaka, Algorithms for radiative intensity calculations in moderately thick atmospheres using a truncation approximation, *J. Quant. Spectrosc. Radiat. Transfer*, *40*, 51–69, 1988.

Nakajima, T., M. Tanaka, M. Yamamoto, M. Shiobara, K. Arao, and Y. Nakanishi, Aerosol optical characteristics in the Yellow Sand events observed in May, 1982 at Nagasaki-PAT II models, *J. Meteorol. Soc. Jpn.*, *67*, 279–291, 1989.

O'Neill, N. T., O. Dubovik, and T. F. Eck, Modified Ångström exponent for the characterization of submicrometer aerosols, *Appl. Opt.*, *40*, 2368–2375, 2001a.

O'Neill, N. T., B. N. Eck, A. Smirnov, O. Dubovik, and A. Royer, Bimodal size distribution influences on the variation of Ångström derivatives in spectral and optical depth space, *J. Geophys. Res.*, *106*, 9787–9806, 2001b.

Öström, E., and K. J. Noone, Vertical profiles of aerosol scattering and absorption measured during the North Atlantic Aerosol Characterization Experiment (ACE 2), *Tellus, Ser. B*, *52*, 526–545, 2000.

Patterson, E. M., D. A. Gillette, and B. H. Stockton, Complex index of refraction between 300 and 700 nm for Saharan aerosols, *J. Geophys. Res.*, *82*, 3153–3160, 1977.

Powell, D. M., J. A. Reagan, M. A. Rubio, W. H. Erxleben, and J. D. Spinhirne, ACE-2 multiple angle micro-pulse lidar observations from Las Galletas, Tenerife, Canary Islands, *Tellus, Ser. B*, *52*, 652–661, 2000.

Pollack, J. B., and J. N. Cuzzi, Scattering by nonspherical particles of size comparable to a wavelength: A new semi-empirical theory and its applications to tropospheric aerosols, *J. Atmos. Sci*, *37*, 861–881, 1980.

Reagan, J. A., M. V. Apte, A. Ben-David, and B. M. Herman, Assessment of aerosol extinction to backscatter ratio measurements made at 694.3 nm in Tucson, Arizona, *Aerosol Sci. Technol.*, *8*, 215–226, 1988.

Reid, J. S., T. F. Eck, S. A. Christopher, P. V. Hobbs, and B. N. Holben, Use of the Ångström exponent to estimate the variability of optical and physical properties of aging smoke particles in Brazil, *J. Geophys. Res.*, *104*, 27,473–27,489, 1999.

Sasano, Y., and E. V. Browell, Light scattering characteristics of various aerosol types derived from multiple wavelength lidar observations, *Appl. Opt.*, *28*, 1670–1679, 1989.

Sasano, Y., E. V. Browell, and S. Ismail, Error caused by using a constant extinction/backscatter ratio in the lidar solution, *Appl. Opt.*, *24*, 3929–3932, 1985.

Schmeling, M., L. M. Russel, C. Erlick, D. R. Collins, H. Jonsson, Q. Wang, P. Kregsamer, and C. Streli, Aerosol particle chemical characteristics measured from aircraft in the lower troposphere during ACE 2, *Tellus, Ser. B*, *52*, 185–200, 2000.

Sokolik, I. N., and O. B. Toon, Direct radiative forcing by anthropogenic mineral aerosols, *Nature*, *381*, 681–683, 1996.

Sokolik, I. N., O. B. Toon, and R. W. Bergstrom, Modeling of the radiative characteristics of airborne mineral aerosol at IR wavelengths, *J. Geophys. Res.*, *103*, 8813–8826, 1998.

Stohl, A., G. Wotawa, P. Seibert, and H. Kromp-Kolb, Interpolation errors in wind fields as a function of spatial and temporal resolution and their impact on different types of kinematic trajectories, *J. Appl. Meteorol.*, *34*, 2149–2165, 1995.

Tanré, D., Y. J. Kaufman, B. N. Holben, B. Chatenet, A. Karnieli, F. Lavenu, L. Blarel, O. Dubovik, L. A. Remer, and A. Smirnov, Climatology of dust aerosol size distribution and optical properties derived from remotely sensed data in the solar spectrum, *J. Geophys. Res.*, *106*, 18,205–18,217, 2001.

Tegen, I., and I. Fung, Contribution to the atmospheric mineral aerosol load from land surface modification, *J. Geophys. Res.*, *100*, 18,707–18,726, 1995.

Tegen, I., A. A. Lacis, and I. Fung, The influence on climate forcing of mineral aerosols from disturbed soils, *Nature*, *380*, 419–422, 1996.

von Hoyningen-Huene, W., K. Wenzel, and S. Schienbein, Radiative properties of desert dust and its effect on radiative balance, *J. Aerosol Sci.*, *30*, 489–502, 1999.

Wandinger, U., and A. Ansmann, Experimental determination of the lidar overlap profile with Raman lidar, *Appl. Opt.*, *41*, 511–514, 2002.

Welton, E. J., et al., Ground-based lidar measurements of aerosols during ACE-2: Instrument description, results, and comparisons with other ground-based and airborne measurements, *Tellus, Ser. B*, *52*, 636–651, 2000.

Wendisch, M., and W. von Hoyningen-Huene, Optically equivalent refractive index of atmospheric aerosol particles, *Contr. Atmos. Phys.*, *65*, 293–309, 1992.

Yang, P., and K. N. Liou, Geometric-optics-integral-equation method for light scattering by nonspherical ice crystals, *Appl. Opt.*, *35*, 6568–6584, 1996.

D. Althausen, A. Ansmann, I. Mattis, D. Müller, and U. Wandinger, Institut für Troposphärenforschung, Permoserstr. 15, 04318 Leipzig, Germany. (dietrich@tropos.de; albert@tropos.de; ina@tropos.de; detlef@tropos.de; ulla@tropos.de)

O. Dubovik, NASA Goddard Space Flight Center, Code 923, Greenbelt, MD 20771, USA. (dubovik@aeronet.gsfc.nasa.gov)

S. Eckhardt and A. Stohl, Technische Universität München, Lehrstuhl für Bioklimatologie und Immissionsforschung, Am Hochanger 13, D-85354 Freising-Weihenstephan, Germany. (eckhardt@forst.tu-muenchen.de; as@forst.tu-muenchen.de)